GUIDING THE NEUROSURGEON IN RESECTIVE EPILEPSY SURGERY

Master Thesis Technical Medicine

Daniël Groothuysen

January, 2019

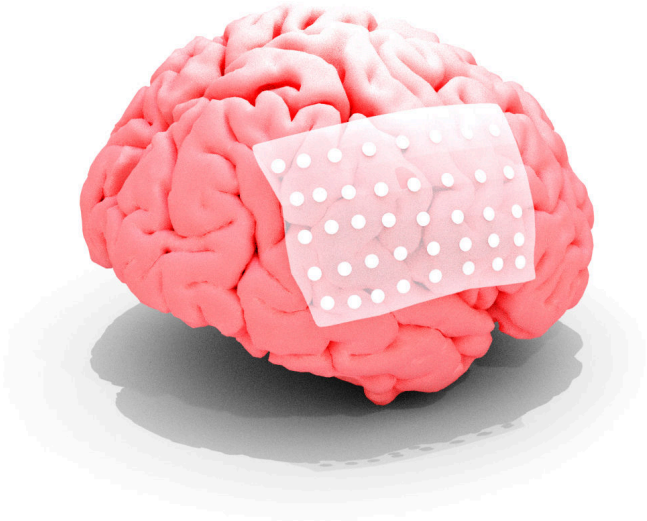

Graduation committee

prof. dr. ir. M.J.A.M. van Putten
dr. G.J.M. Zijlmans
dr. G.J.M. Huiskamp
drs. P. van Katwijk
drs. R.F.M. van Doremalen

UNIVERSITY OF TWENTE.

UMC Utrecht

Research is to see
what everybody has seen;
but to think what nobody has thought.

ARTHUR SCHOPENHAUER

Research is what I'm doing
when I don't know what I'm doing.

WERNHER VON BRAUN

Contents

1 General introduction **9**
- 1.1 Determining the resection area . . . 10
  - 1.1.1 Epileptogenic zone paradigm . . . 10
  - 1.1.2 Network disease paradigm . . . 10
  - 1.1.3 Network measures in epilepsy . . . 12
- 1.2 Image registration of intracortical photographs . . . 14
  - 1.2.1 Research questions and objectives . . . 16

2 Network analysis in chronic ECoG **18**
- 2.1 Introduction . . . 18
- 2.2 Methods . . . 19
  - 2.2.1 Patient population . . . 19
  - 2.2.2 Data acquisition . . . 19
  - 2.2.3 Network analysis . . . 20
  - 2.2.4 Determining resection area and SOZ . . . 21
  - 2.2.5 Statistical analysis . . . 21
- 2.3 Results . . . 22
  - 2.3.1 Patients . . . 22
  - 2.3.2 Visual analysis . . . 22
  - 2.3.3 Network measure results . . . 23
- 2.4 Discussion . . . 24
  - 2.4.1 Comparison with literature . . . 24
  - 2.4.2 Strengths and weaknesses . . . 27
  - 2.4.3 Conclusion and future research . . . 29

3 Image registration of cortex photographs **31**
- 3.1 Introduction . . . 31
- 3.2 Methods . . . 32
  - 3.2.1 Algorithms . . . 33
  - 3.2.2 Validation of algorithms . . . 34
- 3.3 Results . . . 37
  - 3.3.1 Comparison between manual and semi-automatic . . . 37
  - 3.3.2 Effect of collinearity and point spread . . . 40
  - 3.3.3 Registration by non-clinicians . . . 40
- 3.4 Discussion . . . 41
  - 3.4.1 Limitations . . . 41
  - 3.4.2 Future research . . . 42

4 General conclusion **44**

A Technical background for network analysis **46**
A.1 Directed Transfer Function . . . 46
A.2 Network types . . . 48
A.3 Local network measures . . . 49
A.3.1 Strength . . . 50
A.3.2 Betweenness Centrality . . . 51
A.3.3 PageRank Centrality . . . 52

B PageRank plots of unresected patients **54**

C Box plots for all states **55**

D Transformation types **60**

E Extra figures and tables for image registration **64**

F Fully automatic algorithm **66**
F.1 Methods . . . 66
F.2 Results . . . 67

Bibliography **73**

Preface

Na een lange tijd, langer dan ik aanvankelijk had gedacht, ligt deze scriptie dan eindelijk goed en wel voor me. Hoewel deze stage mij enorm veel heeft uitgedaagd en ik het vaak flink moeilijk heb gehad, ben ik trots op het eindproduct wat het me geleverd heeft. Een deel van dit eindproduct is dit lijvige verslag, maar een ander deel is een ook steeds scherper beeld van welke richting ik in wil slaan in mijn verdere carriere. Ik heb ook heel veel geleerd over mezelf en over de enorme complexiteit die de neurologie en het veld van epilepsie biedt. Er is mij weer eens op de neus gedrukt hoe weinig men weet (en daar hoor ik met name bij). Voor mijn gevoel is mijn reis binnen de neurologie nog lang niet ten einde. Ik wil graag een aantal mensen bedanken die me tijdens dit deel van de reis hebben geholpen en onderwezen.

Maeike, bedankt voor de aandacht die je gaf tijdens de vele besprekingen die we hebben gehad; je investeerde er echt in om mijn werkwijze te begrijpen, ook als die soms wat onnavolgbaar was. Ook was je invoelend in de tijd waar ik zoekende was en maakte je dingen goed bespreekbaar en keken we samen naar de opties, wat ik heel fijn vond. Willemiek, bedankt voor je altijd scherpe kijk op dingen en je eerlijke kritiek, en de vele uurtjes in de data duiken, mijn werk is sprongen beter geworden door je hulp. Nicole, ook jij bedankt voor je kritische blik en je ordelijke kijk op dingen alsmede voor de mogelijkheid om echt met patienten aan de slag te gaan en het vertrouwen wat daaruit sprak. Geertjan, bedankt voor het sparren in met name de eindfase van mijn stage en je technische perspectief, alsmede de vele interessante lunchgesprekken over de meest uiteenlopende dingen. Frans, bedankt voor de eindeloos boeiende klinische lessen en een aanstekelijk vuur van enthousiasme over het mysterie van het brein en de waarde van simpele observatie. Michel, bedankt voor het meedenken vanuit Enschede, ook wanneer mijn richting even zoek was, en voor het geven van je ongezouten mening, en vervolgens de geboden ruimte om dingen wel zelf in te vullen. Rob, bedankt voor het zijn van mijn extern lid en voor het mij binnenhalen bij TG als deel van het promotieteam, een eeuwigheid geleden.

Cyrille, bedankt voor het enthousiasme en een inkijkje in de visuele kant van dingen en voor de muziek (helaas dat het Libertangotrio nooit heeft opgetreden), Tineke bedankt voor de kordate hulp en OK-bezoeken. Dorien, Jurgen, Sandra en de rest van de afdeling ook van harte bedankt voor de hulp en gezelligheid! Tessa en Alaitz, bedankt voor het helpen opnieuw leven inblazen van mijn opdracht in een nieuwe richting en een enorm boeiende kijk in het designwerk in Delft, en de fijne lunches in de zon.

Paul, bedankt voor de intervisies die me altijd meer dan genoeg stof tot nadenken hebben geboden, en voor de steun en het uitpluizen van mijn gedachten in de tijden dat het minder ging, en vooral de broodnodige schop achter de kont als ik toch een beetje te weeïg werd. Nienke en Harm, bedankt voor de gezelligheid en steun die we aan elkaar hadden, en de goede, indrukwekkende voorbeelden die ik aan jullie had als laatste van het "intervisienest".

Verder hartelijk dank aan mijn collega's en lotgenoten in de studentenkamer. Emile en Michelle, ik vond het heel gezellig en fijn om naast jullie te werken en ook veel te veel tijd aan raadsels kwijt te zijn (en zoals jullie weten heb ik het nauwgezet bijgehouden)! Ook met mevrouw Banu

was het altijd leuk, ik kom nog een keer rijstevlaai eten. Matteo, grazie per tutti e spero di rivederti presto! Lieke, Erik-Jan, ook leuk om even met jullie in een klein hokje te werken!

Als laatste dank aan mijn vrienden en familie die mij geduldig hebben toegehoord over wat ik allemaal aan het doen was, die mij gesteund hebben in moeilijkere tijden en samen met mij ook successen hebben gevierd! En omdat het zo hoort, als laatste dank aan mijn ouders die mij altijd steunen en ondanks momenten van twijfel hebben geholpen om dit resultaat te bereiken.

Summary

Epilepsy is a debilitating, paroxysmal disease with an worldwide prevalence of 50 million people. Roughly one third of epilepsy patients is refractory and cannot attain seizure freedom through antiepileptic drugs (AEDs). When the epilepsy is focal, these patients can be considered for epilepsy surgery; disconnecting or removing part of the brain to achieve seizure freedom. When no clear focal source such as a tumor or a dysplasia is found, chronic electrocorticography (ECoG) may be used to find the area where the seizure originates; the "seizure onset zone". This is one of the zones used to define the resection, all the while taking into account and avoiding important functional zones.

A **network disease paradigm** has been gaining interest, shifting the thinking from focal zones to networks within the brain that could be disrupted at other places than the place of seizure onset. This network could be characterized by network parameters, quantifying the connectivity of nodes. If this network could be disrupted it would have the profound advantage of being able to spare functional tissue when seizure onset is close to eloquent areas. Furthermore, computing these measures does not necessarily rely on the presence of epileptic spikes or seizures, which makes a larger part of the data usable.

Image registration (transforming images into the same coordinate space) of cortex photographs is a valuable procedure to be able to investigate ECoG data by localizing electrodes and relating data to the anatomical positions of those electrodes. For chronic ECoG, this is already being done automatically by coregistering CTs of implanted electrodes with patient MRIs and locating the electrodes with template matching, but no such automatic method yet exists for twodimensional photographs, and inferences about electrode positions are currently done manually and visually.

In **Chapter 2**, chronic ECoG data of two patients was retrospectively analysed on out-strength, Betweenness Centrality and PageRank Centrality network measures. Per patient, 10 two-second epochs were selected in sleep, containing interictal epileptiform activity. The median network measures for these epochs were computed and for the resected patients (1 and 2), the difference of those measures between resected and non-resected channels is statistically tested, as well as the difference between seizure onset zone and non-seizure onset zone, in a multitude of frequency bands. The most important findings were those in patient 2 with for the resected area higher out-strength and PageRank Centrality in the gamma band. However, visual analysis of the network data shows that the hubs are not always in the resected area. This means that a potential resection based solely on the extreme values of these measures would not overlap with the current resection. While making this new biomarker not yet usable in the current workflow, the question remains whether a resection of these centrality maxima would disturb the epileptogenic network and also effectuate seizure freedom.

In **Chapter 3**, two ways of image registration (manual and semi-automatic) are compared on sets of cortical photographs of 20 patients that have undergone acute corticography. The photograph taken at the beginning of the surgery, after exposing the brain (I_{pre}) is coregistered

with a photograph with an electrode grid (I_{el}) and after resection (I_{post}). The manual task consisted of overlaying in GIMP, a photo editing software. The semi-automatic task consisted of the user clicking three control points per image and the transformation of one image to the coordinate frame of the other being estimated from that. Three clinicians and five non-clinicians performed the manual and semi-automatic tasks. The validation is done with an outcome measure of 16 hand-picked control points per picture, yielding a mean error μ_D for those 16 points within an image pair. For clinicians, $\mu_{D,manual} = 2.02$ mm and $\mu_{D,semi} = 1.78$ mm, which is the same accuracy (no significant increase). However, the semi-automatic task had a significantly lower duration (mean of 132 seconds versus 321 seconds for the manual task), making the semi-automatic procedure superior to the manual procedure, and ready for use in research.

Glossary

SOZ	Seizure Onset Zone
EZ	Epileptogenic Zone
IEMU	Intensive Epilepsy Monitoring Unit
IED	Interictal Epileptiform Discharge
cECoG	Chronic Electrocorticography
aECoG	Acute Electrocorticography
EEG	Electroencephalography
AED	Antiepileptic Drug
DTF	Directed Transfer Function
BC	Betweenness Centrality
PC	PageRank Centrality
MRI	Magnetic Resonance Imaging
CT	Computed Tomography
HF	High Frequency

Chapter 1

General introduction

Epilepsy is a debilitating neurological condition caused by an imbalance between cortical inhibition and excitation. This imbalance can lead to abnormal synchrony of neural activity[1], which often is paired with loss or abnormal excitation of function. These periods of synchronicity are called seizures or ictal periods, and between patients, they vary in frequency, duration, severity, and seizure type. The International League Against Epilepsy (ILAE) classifies seizures into types mainly based on appearance (semiology) of seizures[2]. Seizures are classified as having a focal (limited to a certain area of the brain), generalized, or unknown onset (not witnessed). Subsequently, further distinctions on intact or impaired awareness and motor or non-motor (e.g. speech or sensory) symptoms are made. The World Health Organisation estimates a prevalence of 50 million people worldwide with active epilepsy[3], which is 0.67% of the world population.

The first line of treatment is the administration of anti-epileptic drugs (AEDs). Administering only a single AED is preferred due to the added side-effect burden of multiple drugs [4]. However, guidelines to select the most efficacious and effective initial AED based on seizure type and demographic lack consensus [5] and few randomized control trials investigate additional factors such as safety, tolerability and expense [6]. It is therefore often a personalised and trial-based search to find the appropriate AED for each patient.

Furthermore, some patients cannot attain seizure freedom with AED's alone; failure to attain sustained seizure freedom after two different AED therapies is defined as refractory epilepsy[7]. In a prospective study by Kwan et al., the prevalence of refractory epilepsy in a cohort of 525 patients with various types of epilepsy was 37% [8].

For patients with focal refractory epilepsy, the possibility of resective surgery exists. A recent review by Jobst et al. [9] found a seizure freedom percentage of 58% with epilepsy surgery, as opposed to 8% when continuing AED treatment. The same review found that temporal lobe resection and resection of MRI-visible lesions had the highest chance of post-operative seizure freedom.

The main challenge in epilepsy surgery is to determine the minimal tissue that needs to be resected to disrupt epileptic activity while avoiding functional loss resulting from the removal of too much tissue.

1.1 Determining the resection area

To determine the tissue to be resected, two different paradigms can be broadly described; one that looks at epilepsy as a local pathology of the tissue (an epileptogenic zone or EZ), which is the working model used by neurosurgeons today, and one that views epilepsy as a network disease; a pathological network giving rise to the epileptic activity.

1.1.1 Epileptogenic zone paradigm

The epileptogenic zone is defined as the minimum amount of cortex that must be resected (inactivated or completely disconnected) to produce seizure freedom[10]. Seizure freedom can, however, only be determined after surgery has taken place. Other markers are therefore used to approximate this zone in the pre-surgical workup, consisting of an MRI and video-EEG, and if necessary additional tests such as high-resolution MRI, magnetoencephalography (MEG), and PET or SPECT to investigate metabolism. Invasive recordings of the brain may be used to further confirm the hypothesis of the epileptogenic zone, either by acute electrocorticography (aECoG) to tailor the resection intraoperatively by looking for residual activity, or chronic, multi-day electrocorticography (cECoG). Recently, high frequency oscillations above 80 Hz (ripples) and above 250 Hz (fast ripples) are also measured in corticography[11, 12].

To measure chronic ECoG, subdural electrode grids and strips are implanted in a separate surgery instead of only used intraoperatively, which is the case with aECoG. This enables a multi-day period of functional testing and capture of spontaneous seizures and interictal activity before resection[13]. The onset location of spontaneous seizures, called the seizure onset zone (SOZ), can be measured with cECoG and is the most important approximation of the epileptogenic zone. However, it is unlikely that coverage of the SOZ with the electrode grids is complete[14]. Another zone of interest is the irritative zone(IZ), where interictal epileptiform discharges (IEDs) are generated by hyperexcitable neurons. These discharges are synchronous membrane depolarizations of assemblies of those neurons and are an epilepsy marker. Although they are linked to seizures, the generation mechanisms are believed to be different. Furthermore, the IZ does not necessarily coincide with the SOZ[15], as depicted in Figure 1.2. Additionally, the reaction to single pulse electrical stimulation (SPES)[16] and mapping of motor function, sensory function, and language are also done during cECoG.

The neurologist and neurosurgeon ultimately make a resection plan by combining the congruent information in the pre-surgical workup, sparing as much functional tissue as possible and planning the resection along anatomical landmarks such as sulci.

1.1.2 Network disease paradigm

An alternate paradigm to think about epilepsy is as a *network disease*; a pathological network being the cause of the epileptic activity instead of an epileptic pacemaker in diseased tissue.[17, 18]. This way of thinking opens up other ways to treat epilepsy; disrupting the network may be possible at other locations than the seizure onset zone. This may give clinicians additional tools to preserve eloquent cortex and to resect distant, non-eloquent network hubs instead. For a visual example, see Figure 1.2.

Networks consist of nodes connected by edges; nodes being functional units in a network and edges the connections between them [19]. They can be seen in a multitude of scales and

contexts. Social networks, road networks, airport connections and interneuronal interactions can all be summarized with networks. [20]

It has been known for some time that the brain is a complex network represented on multiple scales. The histologist S. Ramon Y Cajal was the first to describe individual neurons and the micronetwork structures they form[21], and later studies have shown the importance of macroscopic functional networks[22, 23]. The term "connectome" was coined by Sporns et al. to refer to *"the matrix of all possible pairwise anatomical connections between neural elements of the brain"* [24]. Since then, in addition to anatomical connections, matrices of functional connections obtained with various techniques such as functional MRI and electrocorticography have been studied extensively[19].

A functional network of the brain can be constructed on the basis of ECoG data, with the nodes being the electrodes and the edges the *functional connectivity* between them. These electrodes are located on the cortex and measure the *local field potential* of a multitude of neurons in the immediate area of the electrode. This local field potential is largely due to the sum of the synaptic currents of this group of neurons[25]. Functional connectivity is a measure of correlation between two channels; the more two channels influence each other (with either a one way or two way interaction), the higher the connectivity[23].

One of the ways to encode functional connectivity is to compute the Directed Transfer Function (DTF) [26] of the signal; i.e. fitting an autoregressive model to the data to obtain a matrix of connectivity strengths for each electrode pair (For more technical information on DTF, see Appendix A.1). This matrix encodes the connectivity strength of each node i to each other node j; every entry of the matrix, A_{ij}, is the connectivity from i to j. The element A_{ji} encodes the connectivity the other way around. A connectivity matrix and a network are equivalent; the one can be constructed from the other. See Figure 1.1 for an example of a matrix-network pair. If the elements A_{ij} are the same as A_{ji}, then the matrix is symmetrical and the network is *undirected*. If this doesn't hold, then the matrix is asymmetrical and the network is *directed*.

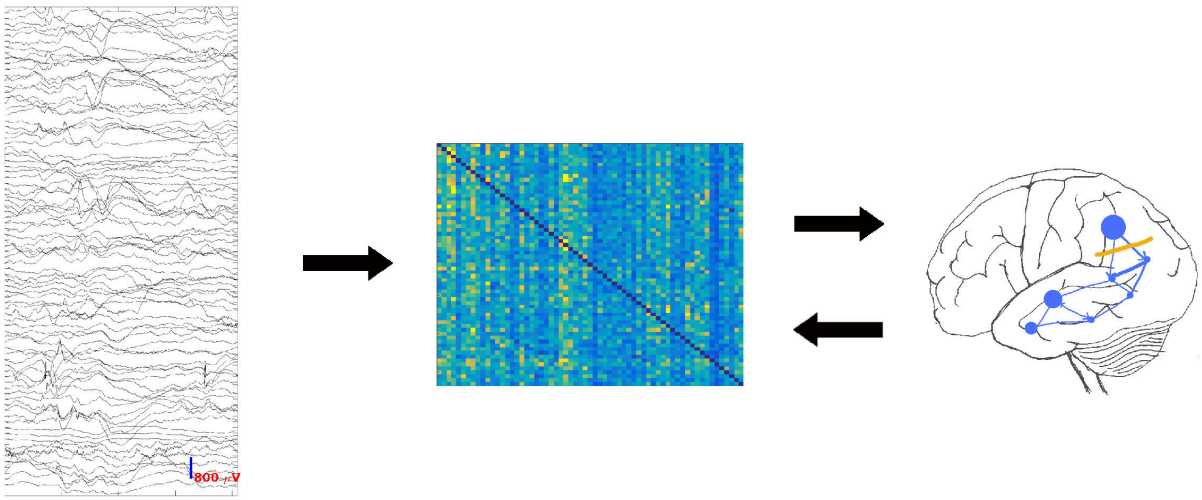

Figure 1.1: Going from measured epochs to a DTF matrix to a network. Encoding the raw data into a connectivity matrix is one-way, but the connectivity matrix and the network are different representations of the network and equivalent.

Connectivity is usually not evenly distributed across real-world networks; some nodes are more connected than others [19]. Once the functional connectivity between the different nodes spread

out over the brain is computed, this information can be used to characterize *hubness* of the tissue. A hub is a highly connected node of a network, and therefore is thought to serve an important role in networks. Hubs can be classified as *connector* hubs which connect different clusters of the network, and *provincial* hubs that are strongly connected within a cluster. For example, in the global airport network, Istanbul is considered the most prominent connector hub, connecting flights from three continents. When this hub would shut down, this will have far-reaching consequences for the network function.[27]. Hub characteristics of the tissue underlying the electrodes can be investigated with *local network measures* called *centrality* measures.

A node's centrality quantifies its hubness because it measures how connected that node is to the rest[19]. This can be an important discriminating measure for epileptogenic tissue. The precise definition of centrality depends on the specific centrality measure used. A multitude of measures exist; we will elucidate three that we will use in this thesis.

Strength is the most fundamental centrality measure; this is simply the sum of the weights of connections going from or to a node. Strength can also be directed: the out-strength and in-strength can be computed. Strength was derived from the analogous parameter in binary networks called degree (simply the number of connections to a node, since every connection can be said to have a strength of one). Opsahl et al.[28] proposed a centrality measure that combines both strength and degree and tunes their relative contribution with a parameter α. This was done to mitigate the problem of the strength of a node with ten weak connections potentially being the same as that of a node with one strong connection. Strength has another problem; it's very local and only takes into account the neighbouring electrodes. Other measures have been proposed that do take into account the whole network; Betweenness and PageRank Centrality are two of those.

Betweenness Centrality (BC) is defined as "the fraction of all shortest paths in the network that pass through a given node"[29] and is an indicator of hub status[30]. For a node k, the Betweenness Centrality can therefore be computed by iterating over all other pairs of nodes i and j, and adding up the instances where the shortest path between i and j crosses k. When a node links two clusters, it has a high Betweenness Centrality because the shortest paths between nodes of the two clusters all go through the linking node. Because the Betweenness value of one node takes into account paths across the entire network, it can be said to take the whole network into account.

PageRank Centrality (PC) is a measure which recursively also takes into account the centrality of nodes adjacent to the node in question to compute its centrality. PageRank Centrality is a variant of Eigenvector Centrality, and is used by Google to rank search results[31]. It has the advantage of being applicable to a directed graph, unlike Eigenvector Centrality. A node has high PageRank Centrality when it is important (has a lot of connections) and is connected to other important nodes; this therefore takes into account the entire network. Such a collection of important interconnected nodes is called a "rich club"[17].

For more technical information on these network measures and an example application on the Dutch railway network, see Appendix A.3.

1.1.3 Network measures in epilepsy

Epilepsy as a network disease has come into view with the advent of depth electrode use in the 1960 by Bancaud and Talairach[32] who found that electrical activity originating from an epileptic lesion did not respect anatomical boundaries and helped introduce the concept of an

epileptogenic network. Since then, studies noted changes in the functional networks during seizures, predominantly in terms of hub status[33, 34], statistically more frequent involvement of anatomical hubs that are affected by epilepsy-generating lesions [35] and altered distribution of those network hubs in networks of cortical thickness [36]. These findings suggest the involvement of hubs in epilepsy, and warrant further investigation of how to use these hubs to improve treatment of refractory epilepsy patients.

Currently, only simulation studies can make virtual resections solely based on network analysis. In a simplified simulation study using four interconnected neuronal populations, it was shown that resecting the "driver" with the most out-strength is a better approach than resecting the hyperexcitable hub [37]. Another simulation study using real ECoG data showed that the virtual resection plan correlated with the actual resection plan in patients with good postoperative outcome[38]. In vivo studies of the efficacy of resecting certain network hubs can only be done by looking at resected patients with good seizure outcome, in the old paradigm of a local epilepsy pacemaker in the EZ. These network measures can be seen as an extra biomarker to determine the EZ; something that could be called a "*pathological network zone*", which could be a combination of various network measures that are found to correlate well with the resection zone.

In a diffusion based MRI tractography study tracking white matter paths according to their water diffusion pattern, patients with idiopathic generalized epilepsy showed abnormal hubs [39]. Furthermore, a cortical thickness network study in patients with temporal lobe epilepsy showed that these networks were changed with respect to controls[36].

In non-invasive functional network studies, a recent MEG study found hubs within the resection zone of the majority of seizure free patients[18], and in another study the same group found low Betweenness Centrality but high interconnectedness within the irritative zone[40]. A third MEG study found postoperative decrease in Betweenness Centrality for seizure free patients[41]. Using EEG measurements, one study succeeded in discriminating children with epilepsy from controls using a multimeasure prediction model incorporating broadband Betweenness and Eigenvector Centrality[42]. Additional resting state fMRI and MEG studies further confirmed the existence of abnormal hubs in epilepsy[34, 39].

Invasive studies use ECoG and depth electrode data to construct a network. Studies focusing on Betweenness Centrality in ECoG as a hub measure have had mixed results. In the interictal state, one study found no role in seizure onset and propagation for nodes with high Betweenness Centrality [43]. Another found high BC in the upper gamma band for resected electrodes in patients with seizure freedom[44]. In ictal data, however, one study found almost no overlap between high-BC nodes and resection[45]. A recent study with 36 patients found worse seizure outcomes when ictal high-BC nodes were resected[46], leading the authors to believe those resected hubs to be protective and inhibit seizures.

Nodes with predominantly outward connectivity in invasive functional connectivity studies have been termed "drivers"[47], defined by the node(s) with the highest out-degree in a study looking at ictal onset network measures; in this study these drivers were always within the SOZ and the resected area. Other ictal studies showed drivers in the form of high gamma-band out-degree in the SOZ and in focal cortical dysplasia lesions[48, 49], and beta and low-gamma out-strength in areas with spikes in depth electrodes[50].

Little is known about PageRank Centrality in invasive epilepsy data. A recent study uses PageRank in ECoG to approximate the SOZ in their "SozRank-algorithm"[51], using a significantly increased value of the Reverse (inflow) PageRank as their hub measure. More studies are done with the related measure of Eigenvector Centrality. Burns et al. found a disconnection

in the form of lower Eigenvector Centrality at seizure onset[52], that coincides with the SOZ. The same Eigenvector disconnection in the SOZ was found interictally in a depth electrode study[53] in the theta band.

Taken together, various local network measures seem to correlate with either SOZ or resection in patients with good outcomes, but there is no strong consensus for some of the network parameters and a large spread of parameter and connectivity measure choices.However, notable trends in results are high out-degree "driver" hubs in the beta and gamma bands within resected and SOZ areas, and low Eigenvector Centrality in the SOZ at seizure onset. Betweenness Centrality results have a less clear trend.

1.2 Image registration of intracortical photographs

The formulation of a resection plan involves incorporating all the different measures and scans into a decision of what tissue to resect. To be able to do that with electrocorticography, it is necessary to relate epilepsy markers measured by certain electrodes to anatomical locations on the brain. Furthermore, it's vital for the resection decision to map the eloquent tissue, which requires the same electrode localization.

Electrodes in chronic ECoG can be localized automatically with CT, when available

When a patient undergoes chronic ECoG, a robust automated method of localizing the implanted electrodes with CT exists[54–56]. This method scans the 3D CT volume with the template of the known CT image of an electrode, yielding the coordinates of the electrodes within the CT image. These CT coordinates are then related to the MRI with automatic coregistration. The last step is to project the electrodes to the cortex to account for the brain shift that may have occurred after implantation. This, however, is only an approximated correction of brain shift.

Brain shift is one of the principal problems in neuronavigation. The factors that cause brain shift can be physical (gravity, patient positions), surgical (fluid loss, resection) and biological (for instance dependent on tumour type)[57]. Neuronavigation links the MRI that is used to the position of the navigation markers on the skull instead of the brain. Therefore, an error is introduced in the navigation whenever brain shift occurs.

CT data is not always available however. In acute corticography there are often multiple situations (positionings) of the grid; it's infeasible and harmful to the patient to make a CT scan for each situation.

Image registration of cortex images is a potential solution for research and surgery

It would be best to link the neuronavigation directly to the visible brain and electrodes during surgery, ideally in real time. This is the most direct way of linking the position of the electrodes to the anatomy and this can also compensate for brain shift. This visual positioning of electrodes would serve two purposes:

1. in the **research environment**, it could be determined which electrodes ultimately were resected with more accuracy, thus facilitating the investigation of the link between markers in the data and epilepsy in patients with successful resection.

2. in the **operating theatre**, data from acute corticography could potentially be visualized on the brain and summaries from multiple grid positions could be displayed at once, facilitating the decision for the surgeon what to resect;

Currently, the different corticography situations are documented with pictures taken by hand. First a picture is taken when the cortex is exposed. Then, subsequently for each position of the corticography grid and after each (partial) resection, a picture is taken.

For acute corticography, the resection is tailored based on epileptogenic markers in the data recorded by the electrode grid[14]. The surgeons remember visually on which parts of the anatomy these pathological channels reside, and then remove the grid and resect, sometimes additionally referring to the pictures that have been taken. In the research environment, photographs of resections and of the grid positions will be overlaid manually or compared side by side to classify electrodes as being resected or not. This method of electrode localization is tedious and error-prone.

Image registration can improve this process of manual electrode localization. In essence, image registration is the transformation of one picture into the coordinate frame of another. This is already being done automatically in 3D to fuse different modalities of brain scans (CT and MRI for instance) to be able to use both when navigating surgically. Automated image registration in 2D has its own challenges due to the inherent deformations of the image projected into the camera due to, among others, perspective changes and lens warping.

Image registration generally consists of these four steps[58]:

1. **Feature detection**: detecting distinctive points on both images that could be used to map one to the other
2. **Feature matching**: matching the detected features of one images to the features of the other
3. **Transform model estimation**: the parameters of the transformation are estimated using the matched points
4. **Image resampling and transformation**: one image is transformed to the coordinate space of the other using the estimated transformation and resampled if necessary.

The transformation model can be selected in advance for an image registration procedure. Selfsimilarity, affine and projective transformations are all linear types of transformations. Non-linear transformations also exist; these can warp an image onto another. More detailed explanation of transformations can be found in Appendix D.

Image registration can be applied in a multitude of fields[58], for instance stitching together multiple photographs to produce a panoramic photograph, combining multiple satellite images into one[59], or detecting changes in a security camera feed. There are also a lot of applications of image registration in the medical field. A survey article by a group in the UMC Utrecht explored these applications in 1998 [60] and gave an update in 2016 [61]. Examples of linear registration are the fusing of CT and MRI for neuronavigation purposes; this is a completely rigid 3D transformation. Examples of non-linear registrations are automatic registration of CT with ultrasound to quantify coronary plaques [62] and registration of the pathological brain with a space-occupying process to a brain atlas [63].

With respect to image registration of intraoperative cortex photographs, little literature is available. Dalal et al.[64] perform intraoperative registration of cortex photographs by using a projective transform and subsequently register them to the MRI. Ruta et al.[65] do describe

the utility of such photographs, but do not mention registration.

In the second part of this thesis, we aim to validate a process similar to in Dalal et al: a "semi-automatic" algorithm where the user chooses a set of control points and an affine transformation is estimated. The aim is to improve the accuracy and consistency of electrode localization and to reduce work load.

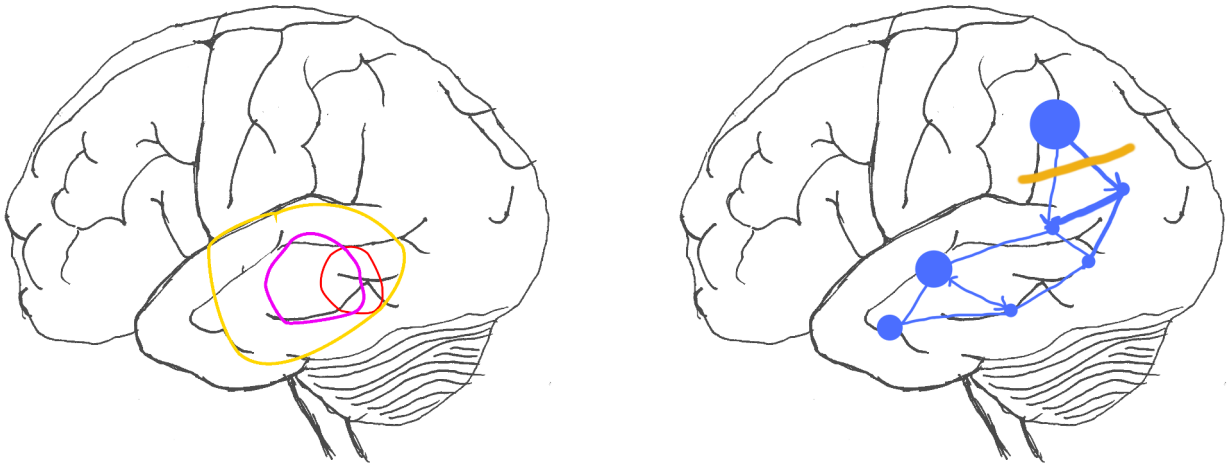

(a) (b)

Figure 1.2: Left: A possible configuration of the different zones is shown schematically. Red is the epileptogenic zone (EZ), magenta is the seizure onset zone (SOZ) and yellow is the irritative zone (IZ). In this hypothetical situation, it can be seen that the SOZ and the EZ do not completely overlap; this might be the case because the measurement only picks up the spreading activity and does not record directly over the tissue that starts the seizure. This might lead to an incomplete resection and is the reason why a margin is taken around the seizure onset zone. **Right:** The same brain with a possible network and a suggested disruption of that network distant from the seizure onset zone. Note that the intervention (orange line) may not be in the same place as the conventional resection plan and therefore opens up new surgery strategies.

1.2.1 Research questions and objectives

To summarize the above, seizure freedom of patients after surgery guided by conventional epilepsy markers is still far from perfect, and the translation from pathological electrodes to location of pathological tissue can be improved, both during surgery and in the research environment.

In this thesis, a future vision will be laid out how better to guide the neurosurgeon in epilepsy surgery. Guiding the neurosurgeon consists of two parts: first finding the diseased tissue more accurately, and subsequently communicating the location of the diseased tissue precisely and clearly. These two parts will be reflected in this thesis in Chapter 2 **"Network analysis in chronic ECoG"** and Chapter 3 **"Image registration of cortex photographs"**.

Taking the above into consideration, we can define two objectives:

- Investigate network measures in interictal chronic corticography data in a wide range of frequency bands in order to make a step towards using network measures as epilepsy biomarkers
- Improve the efficiency and accuracy of the current method of linking data with anatomy.

To this end, we define these research questions:

1. (a) Is there a significant difference between **resected and non-resected** electrodes in terms of out-strength, Betweenness Centrality and PageRank Centrality in chronic ECoG?

   (b) Is there a significant difference between **SOZ and non-SOZ** electrodes in terms of out-strength, Betweenness Centrality and PageRank Centrality in chronic ECoG?

2. Is semi-automatic image registration of acute corticography photographs an improvement with respect to manual registration in terms of accuracy and duration?

Chapter 2

Network analysis in chronic ECoG

2.1 Introduction

Epilepsy is a debilitating neurological disease, affecting approximately 0.67% of the world population[3]. The first line of treatment consists of antiepileptic drugs[4, 5], but a third of patients doesn't respond to pharmacological treatment and is refractory[7, 8]. These patients are evaluated for the possibility of surgery.

When deemed eligible for surgery the pre-surgical workup consists of at least an MRI and EEG, and possibly additional tests[14]. Invasive chronic electrocorticography (cECoG) is a crucial next step when no clear lesion is found[13]. cECoG yields data about seizure onset, interictal spikes and location of functional areas, with which a resection plan is made to resect as much epileptic tissue while keeping functional areas intact, with the goal of inducing seizure freedom or reduction.

However, surgery is no guarantee for seizure freedom; a review stated one-year seizure freedom rates of 53-84% for temporal lobe epilepsy, 36-76% for localized neocortical epilepsy and 43-79% after hemispherectomies[66]. Another study investigating seizure freedom after intracranial EEG (ECoG or depth electrodes) was even more conservative at 58-64% for various epilepsy subtypes[67]. Therefore, there is ample room to improve surgical efficacy.

Network measures are a promising new set of biomarkers to analyse ECoG and a potential improvement to the presurgical workup. Functional connectivity between electrodes can be computed with various correlation metrics and nodes in the resulting functional networks can be quantified with various network measures[23, 29].

Highly connected nodes called hubs are of particular interest[19]. Betweenness Centrality as a measure of hubness is found to be high in resected nodes for the upper gamma band in interictal data[44] but another study found no involvement of the high-BC nodes[43]. Ictally, one study reported worse patient outcome when resecting high-BC hubs[46]. PageRank and Eigenvector Centrality are other measures of hubness which correlate negatively with the SOZ; nodes within the SOZ seemed to be functionally disconnected[52, 53]. Lastly, hubs with predominantly outward connectivity (drivers) as defined by their out-degree or out-strength have been correlated with both the seizure onset zone and resected areas in seizure free patients in predominantly beta and gamma bands[47–49] and with epileptiform spikes in depth electrodes[50].

We expand on this knowledge by analysing chronic ECoG data of epilepsy patients and looking at out-strength, Betweenness Centrality and PageRank Centrality in all the conventional bands

from theta upwards and additionally in the ripple (80 - 250 Hz) and fast ripple (250 - 500 Hz) bands. These bands are chosen because there is still relatively little known about network measures in these bands and therefore it merits further research. Interictal data will be studied; a greater capacity of characterizing epileptogenic tissue in the interictal state will be greatly beneficial to the patient.

This leads us to the following research questions:

1. (a) Is there a significant difference between **resected and non-resected** electrodes in terms of out-strength, Betweenness Centrality and PageRank Centrality in chronic ECoG?

   (b) Is there a significant difference between **SOZ and non-SOZ electrodes** in terms of out-strength, Betweenness Centrality and PageRank Centrality in chronic ECoG?

On the basis of previous studies, we hypothesize that out-strength will be significantly higher in the beta and gamma bands for both SOZ and resected area. Betweenness Centrality is hypothesized to be high in the gamma band for interictal data, and lastly, PageRank is hypothesized to be low for the SOZ.

2.2 Methods

2.2.1 Patient population

We selected patients from the cohort of the MEG-EEG HFO study[68] who had chronic ECoG done in the UMC Utrecht as part of the pre-surgical epilepsy surgery workup, besides other extensive non-invasive electrophysiological workup. This resulted in four patients, two of which were resected on the basis of the pre-surgical workup period; a 17 year old male (patient 1) and a 22 year old female (patient 2), for which patient characteristics can be seen in Table 2.1. The other two patients (patient 3 and 4) were not resected due to lack of a clear seizure onset zone. More on these patients in Appendix B.

2.2.2 Data acquisition

Chronic ECoGs were recorded with grids of platinum electrodes embedded in silicon (Ad-Tech, Racine, WI, USA) with a 128-channel EEG headbox (MicroMed, Veneto, Italy). Only data sampled at 2048 Hz was used. The data was analysed retrospectively.

Epoch selection

The data were visually examined in SystemPLUS Evolution (MicroMed, Veneto, Italy). Noisy channels were visually assessed in ECoG with an amplification of 800 μV/cm and 15 seconds crossover time. Channels with high frequency (HF) noise were also assessed by looking at the signal filtered with a two pass Butterworth bandpass IIR filter with band frequencies of 80 and 500 and order 4, an amplification of 70 μV/cm and crossover time of 2 seconds.

Both noise and HF noise channels were reviewed (by WZ and MZ respectively) and excluded from further analysis. Although the HF noise channels were at first not deemed detrimental,

Table 2.1: Patient characteristics. Age is at inclusion to this study; ED is the epilepsy debut in years of age, Localization is determined localization of suspected EZ after ECoG, TO is temporo-occipital. SOZ well-defined is whether the patient showed a clear seizure onset zone or not. MCD = malformation of cortical development, Follow up is latest follow-up in months in case of resection, #chans is the number of ECoG grid channels (excluding depth electrodes), total versus resected. Engel score[69] is at latest follow-up.

	Patient 1	**Patient 2**
Sex	M	F
Age (years)	17	22
Debut (years)	13	11
Side	Right	Right
Localization	TO	TO
SOZ well-defined	No	Yes
Resection	Maximal temporal lobectomy, hippocampectomy	lateral neocortex basotemporoparietal
AEDs before IEMU	LEV	LEV, LAC
AED stop IEMU	Full	No
Etiology	MCD/MD III	Unknown
Follow-up (months)	13	20
#chans (tot/res)	88/37	72/4
Engel score	IA	IIB

inclusion in analysis showed high network values in these channels and therefore, these channels were also excluded.

For each patient, 40 two-second epochs were selected, consisting of 10 epochs per each of four epoch types, described in Table 2.2. In all selected data the patients had the eyes closed. Awake state epochs were chosen during the day if possible, but sometimes were selected from eyes-closed periods just before sleep (with a maximum of 10 minutes after closure of the eyes). Epochs were chosen to be artefact-free. All epochs were checked by a reviewer (WZ).

Table 2.2: Description of epoch types selected in the data.

Label	Awareness state
A-	Awake state without IEDs (interictal epileptiform discharges)
S-	Sleep state without IEDs
A+	Awake state with IEDs
S+	Sleep state with IEDs

2.2.3 Network analysis

The raw ECoG recordings were preprocessed in FieldTrip by selecting only intracranial channels, excluding the noise and high frequency (HF) noise channels, applying a Notch filter at 50 Hz and rereferencing to the average of the selected channels. Subsequently, the data was cut into the 40 selected epochs, and was converted into z-scores so that the data of each channel has a mean of zero and unity standard deviation.

Per epoch and per frequency band, DTF connectivity matrices were computed with the `DTF` function of the eConnectome toolbox. The bands used were both the conventional bands (δ band from 1 - 4 Hz, θ band from 4 - 8 Hz, β band from 8 - 30 Hz, γ band from 30 - 80 Hz)

and the high frequency bands (Ripple (R) band from 80 - 250 Hz and Fast Ripple (FR) band from 250 - 500 Hz), to be able to compare results to literature. The resulting connectivity matrices $\mathbf{C}_{ijk}$ encode the connectivities from nodes N_j (the sources) to nodes N_i (the sinks), in frequency bin k.

The model order for the DTF was obtained automatically using the eConnectome `arFIT` function by computing, for each epoch, the model order that optimizes the Schwarz Bayesian Criterion (SBC)[70]. The median model order per set of 10 epochs of the same type was taken as the model order for those epochs. This always resulted in a model order of 2.

The frequency bins within one band were averaged to obtain a single twodimensional matrix per epoch and frequency band. Then, the diagonal of this matrix was taken to be the vector of self-connections. Subsequently, the diagonals are set to zero and the out-strength is computed. Betweenness Centrality was computed using the inverse of the connectivity matrix (the connection length matrix), and PageRank Centrality was computed by first symmetrizing the connectivity matrix (adding the matrix to a transposed version of itself). For the PageRank Centrality, the damping factor was set to the default of 0.85; this setting gives a fast convergence[71]. The network measures were computed with the functions `strengths_dir`, `betweenness_wei` and `pagerank_centrality` from the BCT toolbox.

This resulted in a vector of network measures for each combination of seven frequency bands, four awareness states, ten epochs per state, three network measure and four patients (excluding the A+ state for patient 3), totaling 3150 separate resulting vectors.

For visual analysis, the median network measure was taken per channel over the ten epochs of the same state and these median network measures were all individually plotted on a 3D rendering of the segmentation of the cortex of the patients obtained from the MRI. The network measure values were encoded as coloured patches at the approximate location of the electrode. Electrodes obstructed from view in the 3D rendering were displayed next to the cortex, and channels excluded from the DTF analysis were not filled in.

2.2.4 Determining resection area and SOZ

Seizure onset zones for patient 1 and 2 were defined in dialogue with the neurologists in charge of these patients. Generally, a time window of two seconds is used starting from the first gamma activity; electrodes showing oscillatory activity indicative of a seizure within this time period are marked as being within the SOZ.

Based on visual interpretation of presurgical photographs of the grid overlaid on the cortex and postsurgical photographs of the cortex with resected area, electrodes for these two patients were put into one of the following categories: resected, unknown (on the edge of resection or not in view) no contact (when grids and strips would overlap), or not resected.

This method of overlaying the photographs has been developed for this thesis and is further elaborated on in 3.

2.2.5 Statistical analysis

For patient 1 and 2, the median of each electrode category was taken and the significance of the difference of the median network measures was computed using two categorizations: resected

compared with non-resected, and SOZ compared with non-SOZ. Electrodes categorized as unknown or no-contact were excluded from analysis.

A Wilcoxon rank-sum test was performed on the epoch type level, by taking the mean network measure per channel over the 10 epochs in the epoch type, and comparing the two populations (of resected vs non-resected, and SOZ vs non-SOZ). The significance level was chosen with the Benjamini-Hochberg procedure to control for the false positive rate; the p-values were sorted, and the highest p-value that satisfied

$$P_{(i)} \leq \frac{i}{m}\alpha \tag{2.1}$$

was taken as the significance cutoff with m being the total number of tests (112 in this case; two patients, two categorizations, four network parameters and seven bands), i being the rank of the p-value, and $\alpha = 0.05$. P-values lower than or equal to this value were deemed significant.

Analysis was done in MATLAB R2016a (The Mathworks Inc., Natick Massachusetts, United States) in conjunction with the FieldTrip toolbox, version 20160404[72], the eConnectome toolbox version 2.0[1] and the Brain Connectivity Toolbox (BCT) version 2017_01_15[29].

2.3 Results

Results are all in the sleep with events (S+) state; only this state showed significant differences between network measures of resected versus non-resected and SOZ versus non-SOZ electrodes. The data for the other states is shown in Appendix C.

2.3.1 Patients

As stated before, patients 1 and 2 had resective surgery and were included in analysis based on resection area and seizure onset zone. Patient 1 had one subclinical seizure and one stimulation-provoked seizure. The first activity in the subclinical seizure was taken to be the SOZ for this patient; a clinical seizure would be preferable.

For the second patient, the early activity of three different seizures was combined to define a seizure onset zone, this was accorded by the associated neurologist. Patient 1 had a maximal temporal lobectomy and hippocampectomy on the right side; patient 2 had a much smaller removal of part of the lateral neocortex basotemporo-parietally, which was further tailored with acute corticography in the OR. Patient 1 was seizure free at follow-up 13 months after surgery (Engel 1A). Patient 2 experienced a tonic clonic seizure seven months after surgery on holiday during the phasing out of her AED.

Patients 3 and 4 were not resected. Network measures were computed but no significance analysis could be done. Results for those patients are in Appendix B.

2.3.2 Visual analysis

The 3D renderings in Figures 2.1 and 2.2 show examples of network measures, in this case out-strength and PageRank, plotted over the 3D rendering of the segmented MRI of the two

[1] http://econnectome.umn.edu/

analysed patients, in the gamma band and the S+ epoch type (sleep with events). Per channel, the value shown is the median value over the 10 epochs within this epoch type.

Both PageRank and out-strength showed noticably higher values at certain points in the grid, especially near the temporal pole (inside the resection and SOZ) and superiorly in the occipital lobe (within the SOZ). For patient 2, three channels had a notably high value; two of these channels do not fall within the resection however. One of them is at the rostral superior edge of the resection and another is far away from the resection in a strip placed frontotemporally. The high-centrality channel within the resection is relatively higher in centrality in the PageRank measure.

2.3.3 Network measure results

Figures 2.1 and 2.2 show an overview of network measures of electrodes within and outside of groups, where the groups are defined by either resection or seizure onset zone. Results are reported in terms of median network measures over the 10 epochs in a category and median of these medians, hereafter called M for brevity, with M_{in} being the median-of-medians within a zone (resection or SOZ) and M_{out} outside of it.

Out-strength

Out-strength for patient 1 within the SOZ was significantly higher inside of the SOZ in the alpha, beta and gamma band (with (M_{in}, M_{out}) being $(1.1, 0.59)$, $(0.86, 0.45)$ and $(0.48, 0.26)$, respectively). For patient 2 there was an increase of out-strength within SOZ in the beta and gamma bands; (M_{in}, M_{out}) was $(0.79, 0.34)$ and $(0.52, 0.17)$, respectively. Only the gamma band shows a significant difference, the beta band was borderline significant with $p = 0.017$.

Patient 1 seemed to show the same increased out-strength within the resected area relative to outside it, with the maximum at the alpha band ($M_{in} = 0.78, M_{out} = 0.69$); however, this was not significant in the WRS analysis. For patient 2, the resection results closely matched the SOZ results, with again a significantly increased out-strength in the gamma range within the resection compared to outside of it ($M_{in} = 0.61, M_{out} = 0.17$).

Betweenness Centrality

Patient 1 showed a significantly increased Betweenness Centrality in the FR band in the SOZ compared to outside ($M_{in} = 2.92 \times 10^3, M_{out} = 2.40 \times 10^3$). For patient 2, the Betweenness Centrality seemed lower in the SOZ compared to outside, but differences were not significant.

Betweenness Centrality showed no significant difference between resected and non-resected areas for patient 1 and 2.

PageRank Centrality

For patient 1, PageRank Centrality was significantly higher in the alpha, beta and gamma bands in the SOZ compared to outside of it with a (M_{in}, M_{out}) of $(1.52 \times 10^{-2}, 1.16 \times 10^{-2})$, $(1.44 \times 10^{-2}, 1.19 \times 10^{-2})$ and $(1.43 \times 10^{-2}, 1.20 \times 10^{-2})$ respectively. Patient 2 showed a similar pattern, with significantly increased PageRank Centrality in the SOZ compared to outside

of it in the beta, gamma and ripple bands with a (M_{in}, M_{out}) of $(2.13 \times 10^{-2}, 1.44 \times 10^{-2})$, $(2.47 \times 10^{-2}, 1.40 \times 10^{-2})$ and $(2.13 \times 10^{-2}, 1.45 \times 10^{-2})$ respectively.

For patient 1 within the resection compared to outside of it, PageRank Centrality is significant in the beta, gamma and ripple bands with a (M_{in}, M_{out}) of $(1.33 \times 10^{-2}, 1.16 \times 10^{-2})$, $(1.32 \times 10^{-2}, 1.13 \times 10^{-2})$ and $(1.34 \times 10^{-2}, 1.16 \times 10^{-2})$, respectively. Patient 2 showed a significant increase in PageRank Centrality within the resection compared to outside for the gamma band, with a (M_{in}, M_{out}) of $(3.01 \times 10^{-2}, 1.40 \times 10^{-2})$.

2.4 Discussion

In this study, we investigated the difference in three network measures within and out of the resection area, and within and out of the SOZ in two patients with chronic ECoG, measured during sleep in interictal data.

We found significantly higher PageRank Centrality and higher out-strength in the gamma band for patient 2 in the resection, significantly higher PageRank in the beta, gamma and ripple bands but no significantly different out-strength for patient 1, and no significant difference in Betweenness Centrality in the investigated bands. In the SOZ, both patients showed significantly increased out-strength in gamma, and significantly increased PageRank in the beta and gamma bands.

Visual analysis further showed single channels of high centrality (hubs) within both resection and SOZ for PageRank and out-strength. Also outside of these zones, hubs could be found.

If these results are corroborated by more evidence from a bigger cohort, it can be concluded that these network measures have merit and correlate with epileptogenicity. Tailoring the resection with extra information from network analysis could potentially result in smaller resections in the case of patient 1, where one of the channels within the extensive resection has a noticably higher PageRank and out-strength. Furthermore, Patient 2 has a marked hub with high PageRank Centrality midtemporally outside of the resection; it could be hypothesized that if this hub was resected, she would have been completely seizure free. However, it has to be stressed that these hypotheticals are not yet backed up by evidence and more extensive study is needed.

2.4.1 Comparison with literature

According to van Diessen et al., Eigenvector Centrality was low in the SOZ for the theta band, characterizing the SOZ as isolated in terms of EC[53]. We hypothesized that our proxy for EC, PageRank Centrality, would be also low in this band. We did not find a significantly lower PageRank within the SOZ for both of the patients, and the significantly higher PageRank in the higher frequency bands makes functional isolation in the theta band less plausible.

It could be that data for more patients is needed. In the study by Diessen et al., 3 of the 12 patients did show a higher EC value in the SOZ; it could be that this isolating effect is too variable to clearly show with a cohort size of two. Another possibility is that PC gives a significantly different characterization from EC; this could be investigated in further studies by also including EC and directly comparing the two measures.

In literature, out-strength (or its binary counterpart out-degree) is higher within the beta and gamma bands for both SOZ and resection[47–49]. This is corroborated by our data in patient

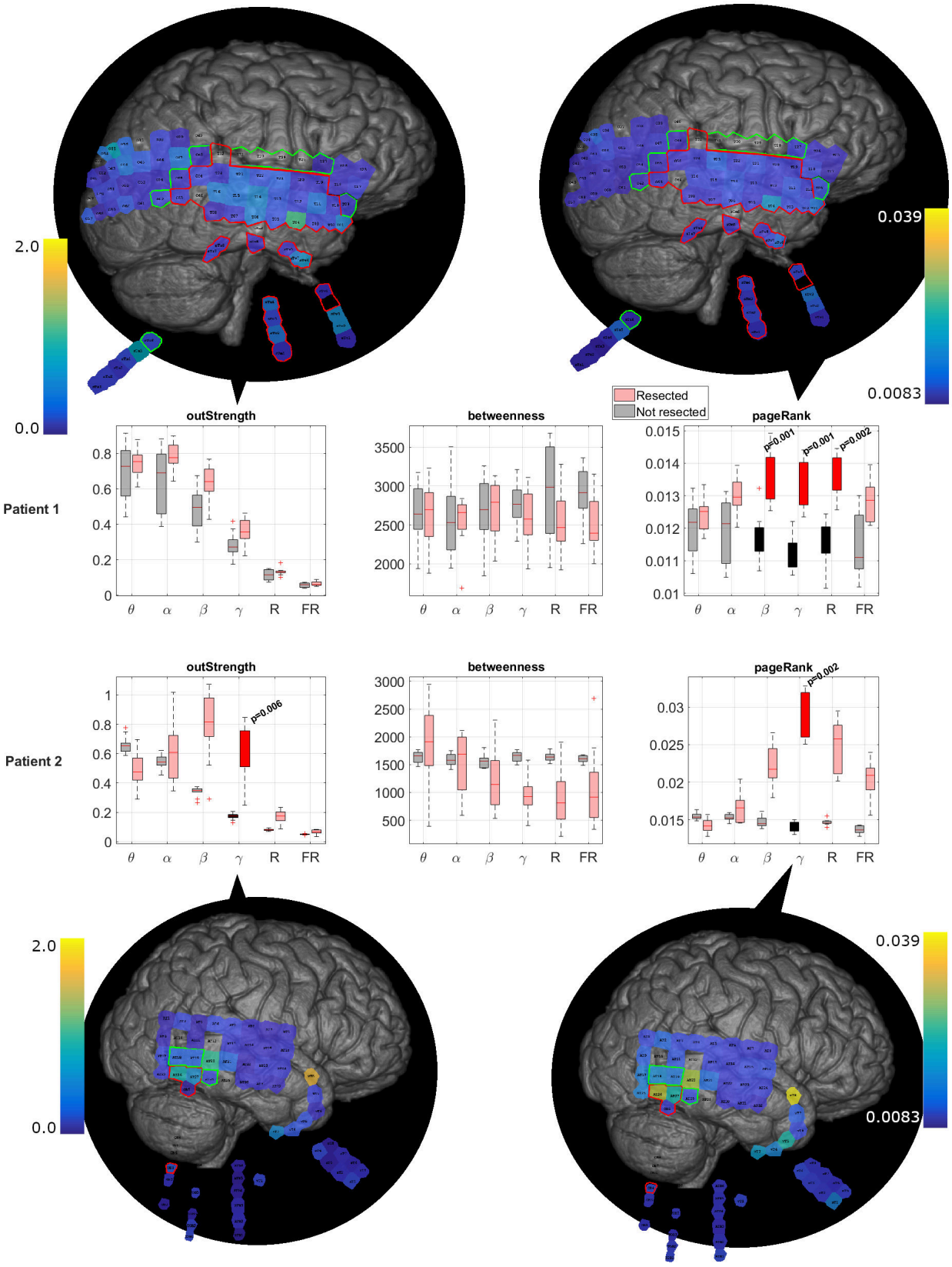

Figure 2.1: Boxplots of median network measures of resection versus non-resection channels in sleep plus events (S+) state. Each box, including its outliers, represents the median network measure of that category for ten separate epochs. Opaque coloring signifies a significant p-value ($\alpha = 7.5 \times 10^{-3}$) resulting from Wilcoxon ranksum analysis, and therefore a significant difference in the values within the resection and outside of it. The significance level was chosen by doing a Benjamini-Hochberg procedure to control the false discovery rate. One of the things that can be seen for patient 2 is significantly increased out-strength and PageRank in the gamma band. Patient 1 had significantly higher PageRank in the resection area for the beta, gamma and ripple bands, although the difference is smaller than for patient 2.

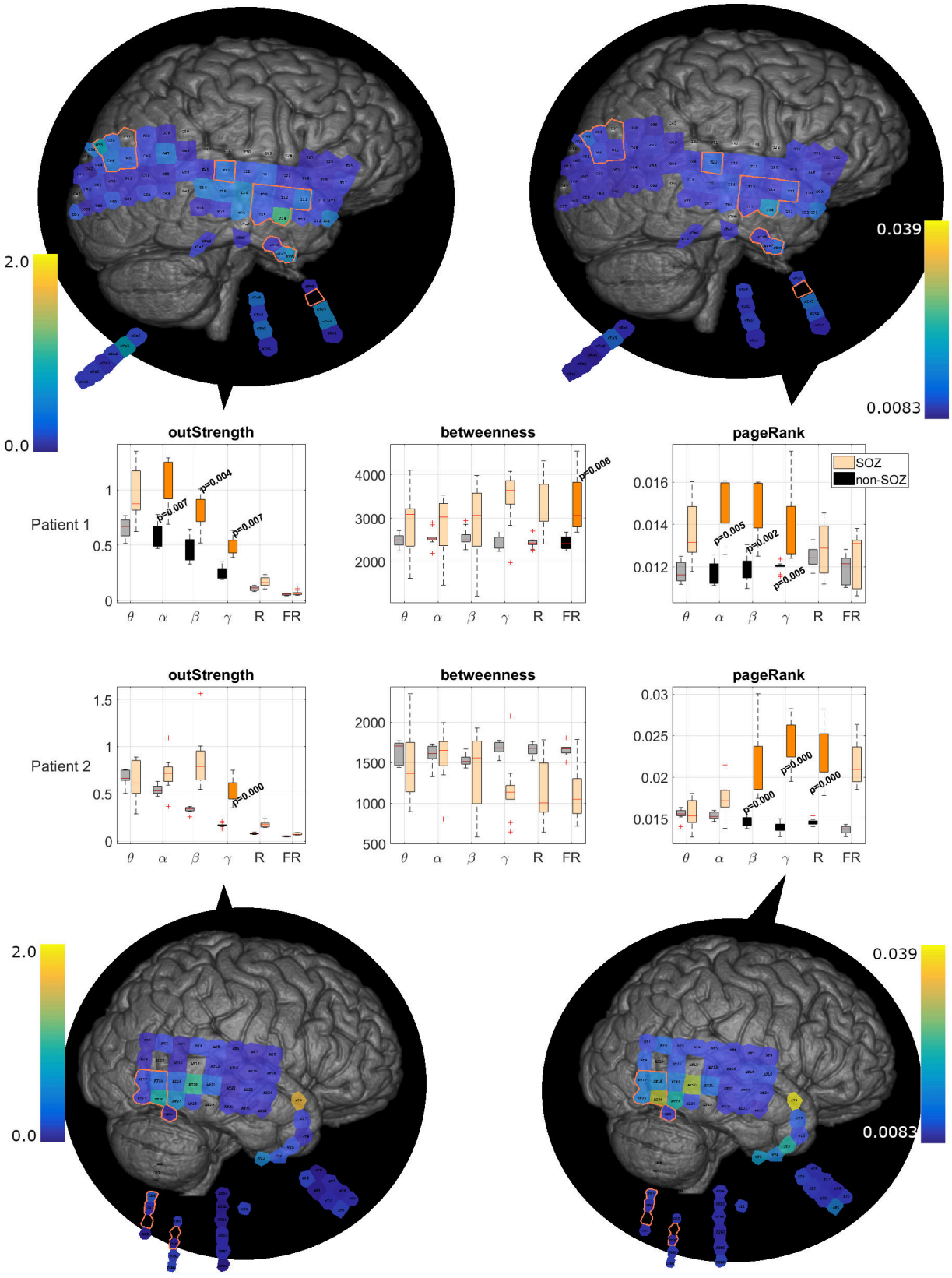

Figure 2.2: Boxplots of median network measures of SOZ versus non-SOZ channels in sleep plus events (S+) state. Each box, including its outliers, represents the median network measure of that category for ten separate epochs. Opaque coloring signifies a significant p-value ($\alpha = 7.5 \times 10^{-3}$) resulting from Wilcoxon ranksum analysis, and therefore a significant difference in the values within the resection and outside of it. The significance level was chosen by doing a Benjamini-Hochberg procedure to control the false discovery rate. What can be seen is that the two highest hubs in the gamma band for patient 1 are both in the SOZ. Some of the hubs for patient 2 are outside of the SOZ, with the most notable being the one in the strip frontotemporally.

2; out-strength is significantly higher in the gamma band in the resection and SOZ. Patient 1 doesn't show the same significance for the resection, but does show a broader range of bands that have a significant increase of out-strength in the SOZ (alpha, beta, gamma). This could be explained by the fact that the two biggest "drivers" of patient 1 (temporally and occipitally) are both within the narrowly defined SOZ, while for the more broadly defined resection, only one of those drivers is included. Because the resection zone is substantially larger, the high out-strength of the temporal driver is diluted. Therefore, it could be said that this data fits with the literature.

Van Mierlo et al.[47] also explicitly looked at the location of the drivers (channels with the highest out-degree) within the zones, showing that for all the 8 patients in that study the driver was in both the SOZ and resection. For patient 1, it can be seen in Figures 2.1 and 2.2 that the driver is indeed located within the SOZ and resection. However, for patient 2 the driver is located within the frontotemporal strip, and even the channel with the second highest out-strength is outside of the resection area, so here it's not the case. This can be explained, however, by the lower Engel score of patient 2 (IIB); this patient possibly could have attained seizure freedom if the drivers were also resected.

Betweenness Centrality was uninformative in our data. The lack of a clear result could be explained by differences in methodological choices; for instance, Ortega et al.[43] use Minimum Spanning Trees to create networks with a subset of the edges whereas in this study, the wholly connected network was used and no thresholding was done. Also, the way of inverting the connectivity matrix may differ, but how this is done is not always reported.

2.4.2 Strengths and weaknesses

Impact of methodological choices

Thresholding of networks In this study, the choice is made to look at the functional connectivity network as a complete network; i.e. that every node is connected to every other node with some non-zero (but potentially near zero) connection strength.

An alternative choice could have been the construction of a Minimum Spanning Tree; a "backbone" of the network which is constructed by including the connections (edges) in order of the strongest to the weakest until all of the nodes are connected, making sure to avoid cycles in the process[17]. A number of network studies in epilepsy use Minimum Spanning Trees[40, 41, 43].

The main problem with weighted, unthresholded networks according to [17] is the introduction of a bias when comparing networks with a different number of nodes N, which is the case in this study. This could then introduce a bias. Because this study looks at significant intrapatient differences between zones and is not a direct comparison of the network measures, this is not estimated to have a big impact on these results.

Choice of connectivity measure In this study, the Directed Transfer Function was used to encode functional connectivity between the channels[26]. This choice has been made to be consistent with previous research, and also because it's a multivariate model which takes into account interaction between all the channels, and is impervious to volume conduction[73].

The disadvantages of this measure are that it is linear and therefore disregards the nonlinear part of the interaction between neuronal populations, that noise in one channel affects the

directional connectivity between that and other channels (which is why noisy channels were excluded in this study) and that indirect connections appear as direct connections in the model (A connection from node $a \rightarrow b \rightarrow c$ could show up as $a \rightarrow c$)[73, 74]. To correct the indirect connections, a normalization with the Partial Directed Coherence could be done, yielding the dDTF (direct Directed Transfer Function)[75].

Focus on interictal data This study chose to focus on interictal data, because the clinical impact of improved tissue characterization in this data is great. Ultimately, this could shorten the patients' stay in intensive monitoring units while implanted and would be a boon to patients with few spontaneous seizures, as confirmed by Korzeniewska et al.[76].

Arbitrary methodological choices A number of methodological choices is made that need further investigation. The Schwarz-Bayesian Criterion (SBC) is used to determine the DTF model order, which always was set to 2. This means that the MVAR model maximally includes signals that are $\frac{2}{f_s}$ samples in the past. This could lead to a limitation in how far-reaching connections can be. However, we chose to stick to the value given by the SBC.

Epochs are chosen to be two seconds long. This length of epoch is taken to try to ensure stationarity of the signal, which is a prerequisite of DTF[26], and to be able to select epochs that are artefact free.

Data was collected from a sleep state, and epochs were selected with interictal spikes present. Epoch sets for three other states were also selected, but sleep with interictal events seemed to give the biggest discriminatory power and by far the highest statistical significance in the differences between zones. See Appendix C for box plots of all states.

Confounding effect of lobes

When looking at differences of median network measures between areas, these differences do not necessarily have to arise from pathological tissue. The brain can be safely assumed to be heterogeneous with respect to network measures over the cortex.

When measuring within a small area this does not pose a problem as this heterogeneity will probably be small. However, the resection of patient 1 was a maximal temporal lobectomy and therefore it cannot be discounted that differences in network measurements between lobes could be a confounding factor in this patient; the division between resected and non-resected is also effectively a division between temporal and parieto-occipital regions.

A way to correct this could be to only measure differences within one lobe, but that would not be possible for a patient such as patient 1. Another way could be to define a mean network "map" mapping several network measures over a large number of patients and normalize with that map. However, this would only work if the distributions of network measures were similar accross patients.

Potentially imperfect resection

Because of the circular definition of the epileptogenic zone as the minimum amount of cortex that produces seizure freedom after resecting it[10], there is no gold standard for epileptic tissue. In literature, the two most used approximations are the zone where seizures originate (SOZ)

and the resected tissue in patients with seizure freedom. We look at both these approximations. However, the resections of these two patients are illustrative of the problems that can arise with using the resection approximation.

Patient 1 underwent an extensive temporal lobectomy with hippocampectomy and therefore the resection is very likely to also contain healthy tissue. Therefore, the median network measure in the resected area becomes less of a good characterization of abnormal tissue.

Patient 2 experienced one major seizure after surgery whilst on holiday and in the process of tapering off from her AEDs, leaving the possibility open that not all the epileptogenic tissue is resected. This makes the median network measure in the non-resected area less of a good approximation of the median network measure in healthy tissue, as pathological hubs may be present in the non-resected tissue.

Complexity and low number of cases

The MEG-EEG HFO cohort was chosen because of the initial plans of comparing these three modalities on the same locations. However, the intersection between this cohort of 37 patients and the group of patients that underwent a chronic ECoG at the IEMU was unfortunately small (n=4).

Furthermore, these four patients were complex cases, with patient 3 and patient 4 not being resected at all after the IEMU period because of insufficient evidence for localization. Patient 1 had diffuse activity over a big region and therefore a big resection was done, which for this study can be detrimental to the results as there might be variation in epileptogenicity within the resection. This will dilute the difference between network measures within and outside of the resected area. Patient 2 was clinically the most suitable patient, with a small resection and near seizure freedom at the end.

Ideally, a large group of patients with clear focal cortical dysplasias and seizure free outcome would be examined, but unfortunately such a cohort was not readily available.

2.4.3 Conclusion and future research

In conclusion, this study suggests that out-strength and PageRank Centrality in the gamma band for interictal data are good candidates for biomarkers of the epileptogenic zone. Drivers and hubs are generally within the resection zone and also are included in the seizure onset zone. However, they are also found outside of these zones. This could point towards an incomplete resection, or the hub could be physiological. Further research is needed to be able to make this distinction.

The ultimate goal would be to base resection strategies on network analysis measures; this could result in narrower, more tailored resections (in the case of patient 1) or more complete resections (in the case of patient 2). The fact that these hubs can be found interictally is also encouraging and could spare time in the intensive monitoring unit for patients with sparse spontaneous seizures.

However, extensive further research is needed before clinical trials could take place that investigate the real added value of this new biomarker; some suggestions for further research avenues are given here. Firstly, a bigger patient cohort is needed with simpler pathologies and complete

seizure freedom, i.e. for whom the resection area is a better approximation of the epileptogenic zone. Then, network parameters could be linked more confidently to epileptogenic tissue.

Furthermore, arbitrary methodological choices like choice of connectivity measure, epoch length and other model parameters still have to be made and need to be based on evidence. There are, broadly speaking, two avenues to determine the correct choices; either driven by domain knowledge or data-driven.

Domain knowledge-driven choices would depend on pathophysiology to determine things like model order. By contrast, a data-driven approach would try to maximize discriminatory power to determine the EZ for a certain data set by tuning the parameter set of methodological choices. Because these parameters are interdependent, the search space is large. This maximization could be done by a machine learning algorithm that searches this parameter space to find that set of parameters that can best help discriminate epileptogenic tissue with network parameters.

Chapter 3

Image registration of cortex photographs

3.1 Introduction

Refractory epilepsy is sometimes treated with surgery in combination with electrocorticography[14, 77]. Either chronic ECoG with previous implantation or acute (intraoperative) ECoG can be used. During resective surgery, the clinical neurophysiologist aids the surgeon by measuring an acute corticogram and interpreting the measured data to tailor the surgery. The positions of the grids on the cortex are recorded by taking pictures with a handheld camera, for later clinical documentation and research. If the patient also underwent chronic ECoG, then the same photographs were taken during the implantation surgery.

Both inside the OR, and outside of the OR in the clinical or research setting, there is a need to relate the positions of the electrodes to the anatomy. For chronic ECoG, this is necessary to interpret results during the registration week, and for acute ECoG this is necessary within the surgery to help tailor the resection, and in the research setting to study acute ECoG data.

For chronic ECoG, there is the possibility of performing a CT to automatically localize the implanted electrodes[55, 56, 78], which is routinely done with good accuracy. The electrodes produce a known signal in the CT and the locations can be automatically found in the CT space by matching a template of an electrode with the data. The CT is then coregistered (matched) with the MRI and then the electrode positions are available in MRI space for further processing. One challenge in this coregistration and electrode localization is brain shift. This is the non-linear deformation of the brain due to patient position, inflammation after implanting the electrodes, or different levels of cerebrospinal fluid[57]. Localization algorithms correct for this by projecting the electrode positions to the cortical surface in MRI space[54, 79].

For acute ECoG, a CT cannot be done intraoperatively. Photographs are taken of each position that the grid is in while the tissue is iteratively resected by the surgeon and then measured by the clinical neurophysiologist, to try and remove only the pathological tissue.

After the surgery, researchers are faced with the task of relating different grid positions to a photograph of the clean cortex, or classifying electrodes on the grid to be resected or not. Currently, this is done by either manually coregistering the photographs in image manipulation software, or not coregistering at all and obtaining the information with a side-by-side view.

Image registration has many applications outside of medicine, in for instance stitching satellite images together automatically[59], but also making a panoramic picture with a phone or

analyzing movement on security footage[58]. In the medical field, it can for instance be used for automatic coronary plaque quantification[62], automatic segmentation of brain lesions[63] and aforementioned CT-MRI coregistration[61].

Since the current workflow of manually coregistering or side-by-side viewing to localize electrodes is cumbersome and potentially error-prone, we propose a semi-automatic algorithm with user input of three control points to perform this coregistration and compare it to manual coregistration in terms of accuracy and duration.

This is expressed in the following research question:

2. Is semi-automatic image registration of acute corticography photographs an improvement with respect to manual registration in terms of accuracy and duration?

It is hypothesized that the semi-automatic algorithm will have a shorter duration. Dalal et al. [64] performed a similar coregistration of photographs with MRI data which yielded a mean discrepancy of 2.0 mm with six electrodes used to compute a projective outcome. We hypothesize results from 2 - 5 mm, due to our lower control point count. Because the accuracy of manual overlay has not been tested, it is not known whether this is an increase with respect to manual overlay.

3.2 Methods

This substudy will explore a **semi-automatic** image registration technique and compare it to an approximation of the current workflow, **manual overlay** in image editing software (see Figure 3.1)

This is done on 20 sets of pictures, each set corresponding to a patient who has undergone surgery combined with acute ECoG in the UMC Utrecht hospital. Each set contains three images: an image of the "naked" brain before starting the procedure (I_{pre}), an image with one or multiple electrode grids (I_{el}) and an image after resection (I_{post}). See Figure 3.2a for the three images of patient 3.

These two image registration approaches have the same aim: to transform one image (I_{moving}, since it is the one being transformed) to the coordinate frame of another image (I_{fixed}). Expressed mathematically:

$$^{M}\mathbf{p} \mapsto {}^{F}\mathbf{p} \tag{3.1}$$

where $^{M}\mathbf{p}$ denotes the set of coordinates of the to be moved image in twodimensional space, and $^{F}\mathbf{p}$ the coordinates of the fixed image where the moved image is transformed towards. Performing a linear transformation then amounts to finding the correct transformation matrix $^{F}\mathbf{T_M}$ from coordinate frame F to M so that:

$$^{F}\mathbf{T_M}\,{}^{M}\mathbf{p} = {}^{F}\mathbf{p} + \mathbf{E} \tag{3.2}$$

The error term E is introduced because the linear transformation cannot completely fit one coordinate system to another if the required transformation is non-linear.

The accuracy and time spent for each of the two methods (manual and semi-automatic) will be evaluated, and a suggestion will be made for the algorithm that has an optimal time/duration combination.

3.2.1 Algorithms

Manual overlay

The manual overlay task is a model for the current workflow of the clinicians and researchers. In the current workflow, either an overlay is made in a photo-editing software to be able to see what parts of the cortex were resected (or to map a photo onto a rendering), or the location of the electrodes is inferred by looking at the pictures side-by-side.

This workflow is modelled in this validation by having the user overlay both the I_{el} image and the I_{post} image onto the I_{pre} image by translating, rotating, scaling and shearing the images with a computer mouse in the open source software GIMP. Essentially; the user performed an affine transformation. For more information about transformations, see Appendix D.

The scaling was not limited to a fixed aspect ratio; both dimensions could be independently scaled. The only prohibited operation was a perspective transform, since otherwise the transformation would not be affine anymore. The reason to perform an affine transformation is to limit distortions when the chosen control points are too collinear. See Figure 3.3a for an example of a manual overlay task.

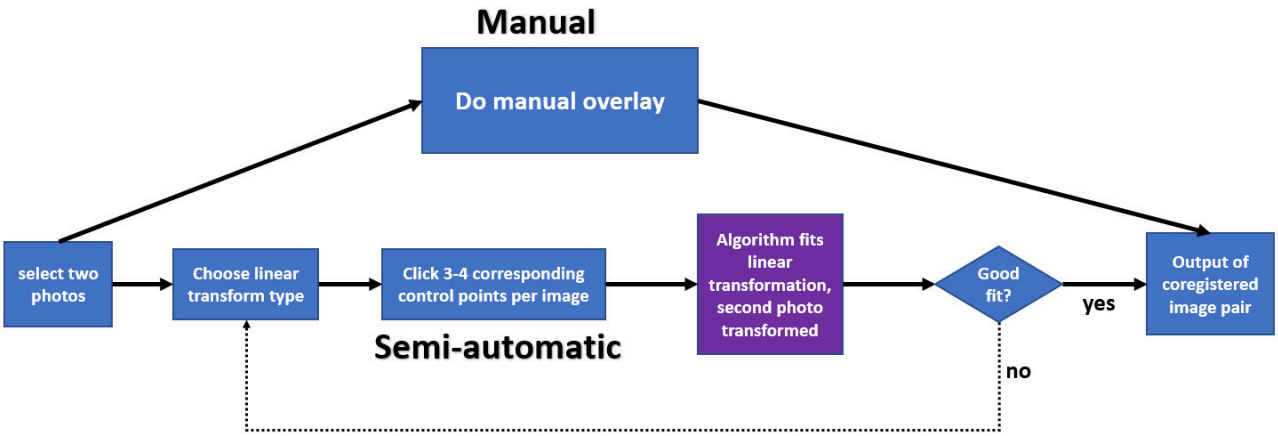

Figure 3.1: Schematic representation of the two image registration methods that are evaluated, the manual (upper branch) and semi-automatic (lower branch) method. A blue block signifies user input and a purple block corresponds to an automatic process. If the fit is visually deemed low at the end by the user, a new transform type may be attempted.

For the steps of the different proposed algorithms, see Figure 3.1.

Semi-automatic algorithm workflow

For the semi-automatic algorithm, the user is presented with an interface to select the two photos that need to be registered.

Subsequently, the user is presented with the two selected photos side by side and defines 3 corresponding control points on the cortex shown in both images. The user is instructed to refrain from choosing collinear points and to try and spread out the points as much as possible to reduce error rates.

The algorithm then computes the linear transformation by solving a system of linear equations as outlined in section D.

At the end, the user checks manually if the fit is deemed good enough; when determining resection classification of electrodes for research purposes, this fit particularly needs to be good in areas near the resection. If the fit is not sufficient, other control points can be chosen (for instance less collinear or closer to the resection).

3.2.2 Validation of algorithms

Outcome measure

To be able to compare manual and semi-automatic overlay, an outcome measure needs to be defined. We have chosen to hand-pick a set of points on the images that we can confirm are the same in both images, so that if the transformation of one image into the other coordinate frame is done, the distance between the hand-picked points in the fixed image and the transformed image will be the local measure of how well the two images match.

For each of the image pairs that are used for the validation, 16 corresponding control points are manually selected by the researcher as uniformly as possible on the cortex. The mean distance or error per control point pair μ_D then acts as a goodness-of-fit parameter with which registrations can be evaluated; this is the outcome measure.

Mathematically, μ_D can be expressed as:

$$\mu_D = \frac{\sum_{n=1}^{16} ||m_n - f_n||}{16} \tag{3.3}$$

where m_n corresponds to the nth point of the 16 outcome control points in the transformed or "moving" image (this being I_{el} or I_{post}) and f_n the nth point of the outcome control points in the fixed image (I_{pre}). For each pair of points, the euclidean distance is computed between the points and all of the distances are meaned.

This μ_D will be expressed in pixels and in millimeters. The conversion to millimeters is done by using the electrode grids on the I_{el} images as a reference; the interelectrode distance is exactly 1 cm. Up to nine electrodes were pinpointed in every electrode picture by the researcher and the mean distance of those nine electrodes measured (pairwise, along the lines of the grid so as not to measure a diagonal).

Clinician validation

Three clinicians performed both the manual overlay task and a semi-automated overlay task for all 20 patients. Two image pairs were assigned for registration per task: the $I_{pre} - I_{el}$ pair and the $I_{pre} - I_{post}$ pair. All images are then transformed to the coordinate system of the I_{pre} image.

After these manual and semi-automatic overlays, the mean error μ_D is computed per task and patient. The time spent by the clinicians for each task is also recorded.

Effect of collinearity and point spread

When performing the semi-automatic overlay, users are free to choose the control points where they want on the cortex. They are instructed to not place them collinearly, and spread them

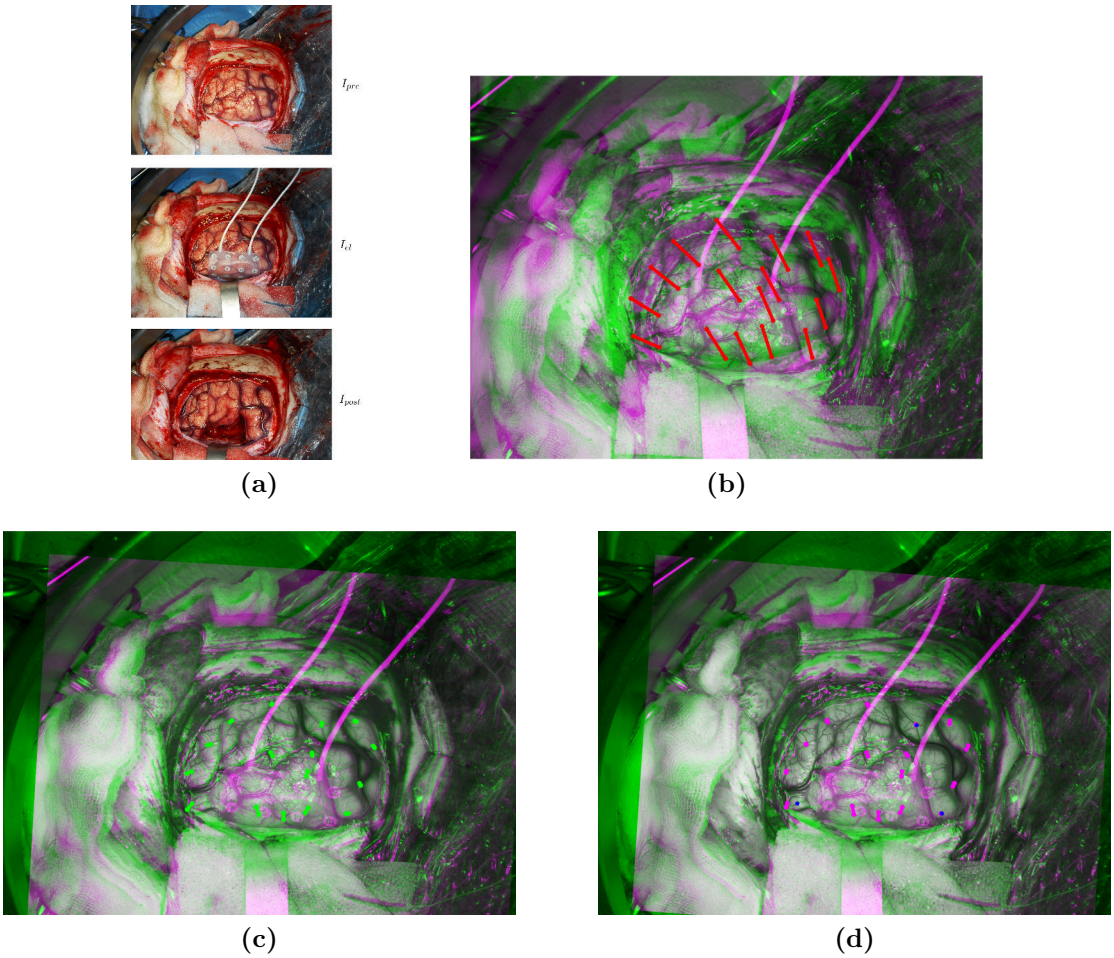

Figure 3.2: **(a)** From top to bottom, these are the I_{pre}, I_{el} and I_{post} images for patient EP_03. These photos are taken at the start of surgery but after trepanation, after placement of an electrode grid, and after resection respectively. **(b)** For the same patient, this is a fused view of the I_{pre} and I_{el} images with I_{pre} shaded in green, I_{el} in magenta and areas with similar colors in grayscale. Manually, 16 points have been selected by the researcher on both images, and these points are connected with red lines, making visible the initial mismatch between the two pictures. **(c)** The same fused view, but after the manual task by clinician 2. The errors between the same 16 points are now shown in green. **(d)** The same image pair after the semi-automatic task of clinician 2. Errors are shown in purple and the three control points that have been clicked in blue. Naturally, because pairs of three points are fitted, those control points have zero error, as the algorithm fitted the images to minimize those errors. If more than three points are fitted, this zero error for the control points is not guaranteed.

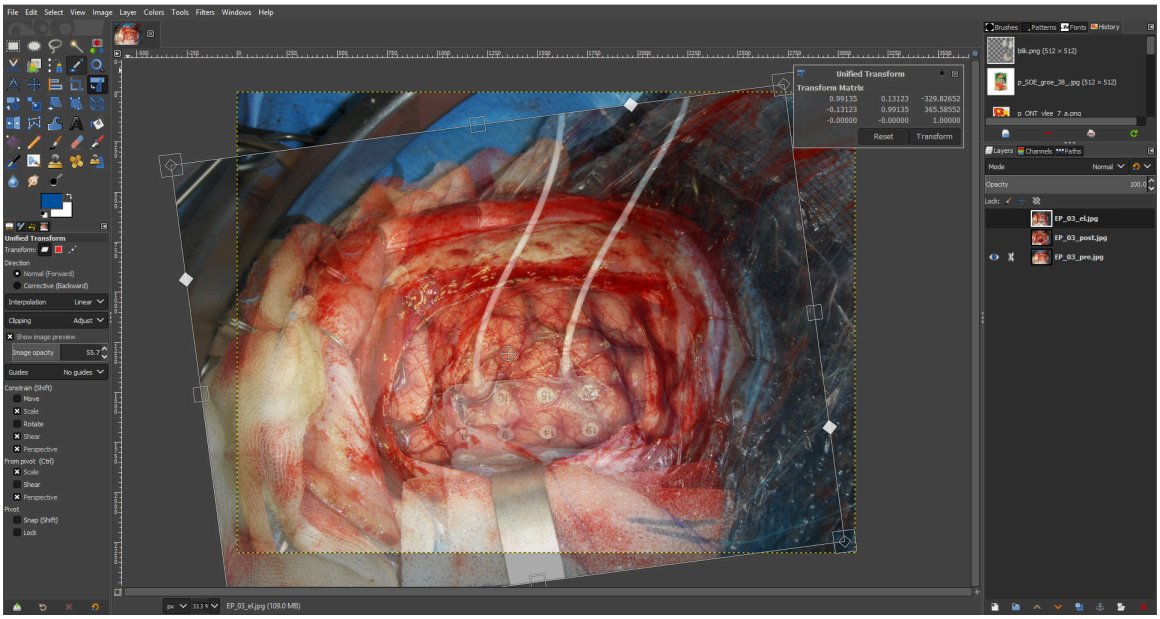

(a)

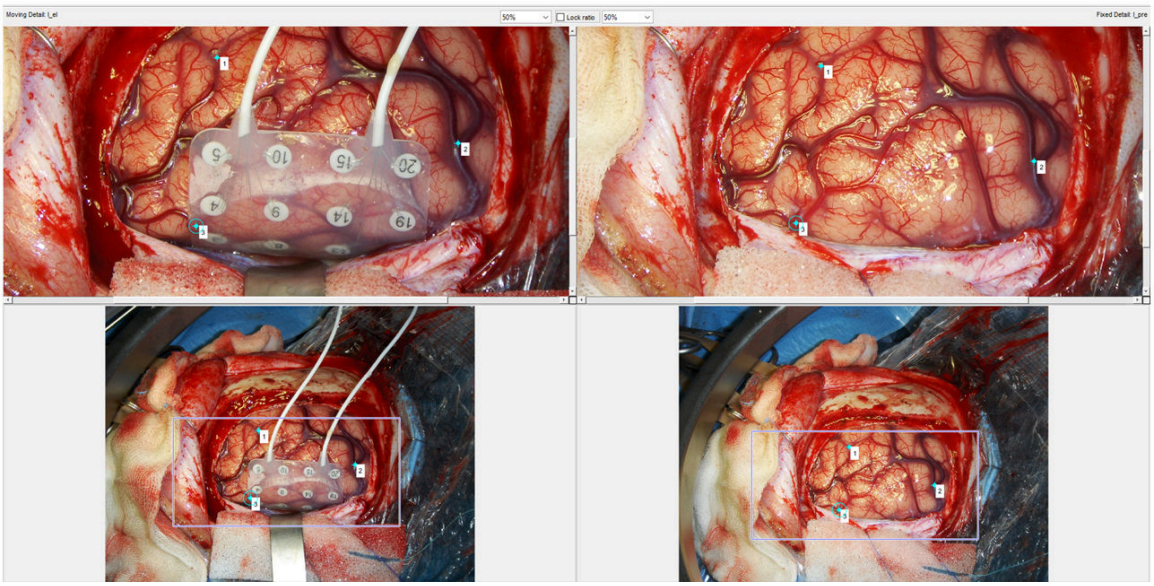

(b)

Figure 3.3: (a) Example of an overlay task in GIMP. Here, the electrode image is being manipulated to be in the same coordinate frame as the underlying clean brain image. The operations that are being used are translation, rotation, (ratio-independent) scaling and shearing. (b) Example of a semi-automatic task of the same image pair in MATLAB. The user selects a minimum of three control points that correspond between the two images, so that a registration algorithm can then put the two images in the same coordinate frame.

out as much as possible while still placing them on the brain.

To measure the effect of these two things, a collinearity measure *coll* and the area of the triangle A formed by the control points will be computed. If we label the lengths of the three edges of the triangle as e_1, e_2 and e_3, the collinearity is defined like this:

$$coll = \frac{2e_a - (e_b + e_c)}{e_a} \tag{3.4}$$

$$e_a = \max_i e_i \quad \forall\ i\ \in \{1, 2, 3\} \tag{3.5}$$

where e_a is the length of the largest edge of the triangle and e_b and e_c are the lengths of the other two. This collinearity measure will vary between 0 and 1; it will be 1 if $e_b + e_c = e_a$ (when the three vertices of the triangle are aligned), and 1 if $e_a = e_b = e_c$, when the control points form an equilateral triangle.

The area of the triangle is computed with the MATLAB function `polyarea`.

Non-clinician validation

In addition to the validation by clinician, five non-clinicians are also asked to perform the manual and semi-automatic overlay on three patients in the same way, and the result compared with clinician performance.

Because of time constraints, three patients were chosen for the non-clinicians to perform the manual and semi-automatic overlay on, namely EP_02, EP_04 and EP_06. These values will be compared with the values of the clinicians for these three patients. Non-clinicians were students of industrial design, civil engineering and physics recruited at the TU Delft university; none of these non-clinicians had a medical background.

3.3 Results

3.3.1 Comparison between manual and semi-automatic

In Figure 3.4, μ_D of the manual and semi-automatic overlay tasks for the 20 validation patients are plotted, as performed by the three clinicians. The left plot shows the accuracy for the $I_{el} - I_{pre}$ image pair, and the right plot for the $I_{post} - I_{pre}$ pair.

Table 3.1 shows a summary of the validation data for the three clinicians, for both the manual and semi-automatic tasks. The duration data for clinician 3 is not used because it contained too many outliers. In this table, it is shown that the μ_D for the semi-automatic tasks, expressed in mm and pixels, are both lower than for the manual task. However, this decrease is not significant (one-sided t-test, $p = 0.095$). The decrease in duration of the semi-automatic task with respect to the manual task, however, is significant (one-sided t-test, $p = 0.000$).

In Figure 3.5, the μ_D for the two image pairs are summed and plotted as a function of their duration. It can be seen that the semi-automatic data cluster has a noticably lower duration than the manual, and seens to also have a generally lower mean error. The right plot shows the same data but this time, the accuracy and duration of the manual task for each patient

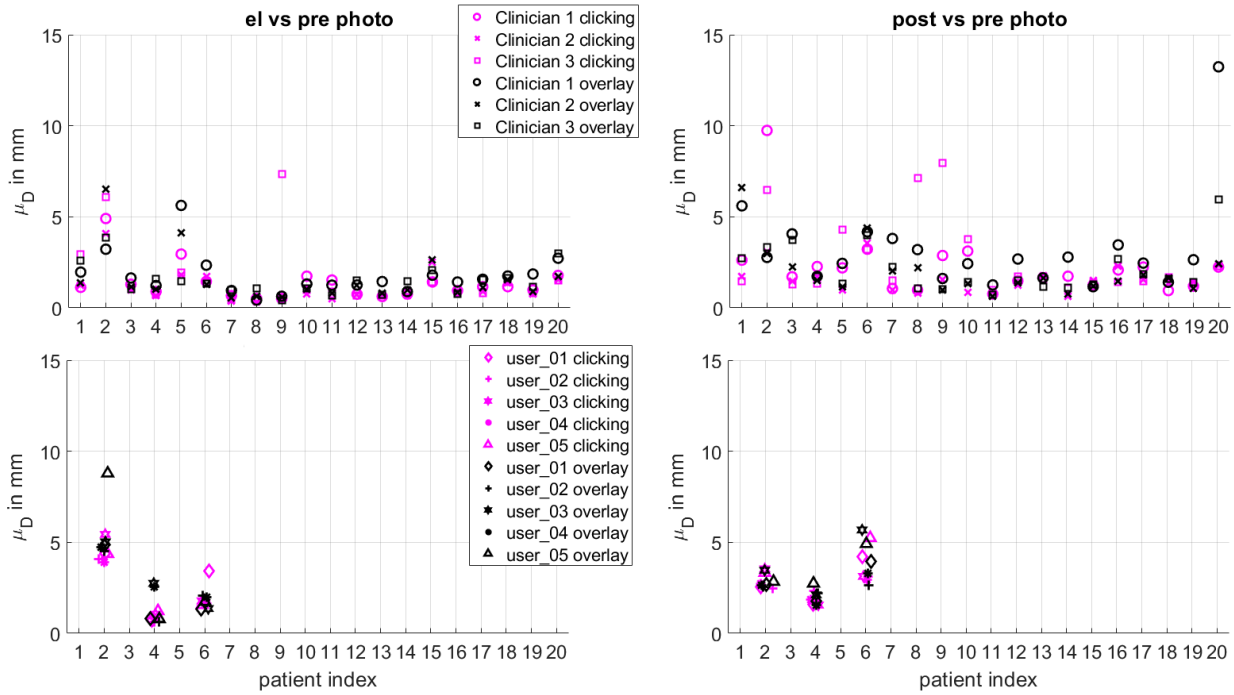

Figure 3.4: Top: Accuracy in terms of μ_D for three clinicians, plotted as a function of patient index. The left plot shows the accuracy for the $I_{el} - I_{pre}$ image pair, and the right plot for the $I_{post} - I_{pre}$ pair. The magenta points represent the semi-automatic task and the black points represent the GIMP manual task. A mean difference in error rate per patient is visible, suggesting that some patients are more difficult than others. **Bottom:** The same plots for the five non-clinicians.

is centered on zero; the relative μ_D and duration is plotted. Seeing as most points are in the lower left quadrant. This means that in general the semi-automatic tasks had a smaller μ_D and shorter duration than the manual task.

Table 3.1: μ_D and duration (reported as mean ± standard deviation over the 20 patients) for the manual and semi-automatic tasks for the three clinicians that performed the task, as well as the total mean. There is no significant decrease in μ_D for semi-automatic as opposed to the manual task (one-sided t-test, $p = 0.095$). However, semi-automatic is significantly faster (one-sided t-test, $p = 0.000$), *

		clinician 1	clinician 2	clinician 3	total
Manual	μ_D [mm]	2.50 ± 2.12	1.76 ± 1.40	1.80 ± 1.12	2.02 ± 1.63
	μ_D [px]	52.75 ± 33.57	38.17 ± 27.91	38.38 ± 19.80	43.10 ± 28.29
	duration [s]	252 ± 89	389 ± 163	–	**321*** ± 147
Semi-automatic	μ_D [mm]	1.81 ± 1.57	1.36 ± 0.84	2.17 ± 2.04	1.78 ± 1.58
	μ_D [px]	40.16 ± 34.74	30.12 ± 18.77	51.26 ± 56.75	40.51 ± 40.51
	duration [s]	107 ± 39	156 ± 37	–	**132*** ± 45

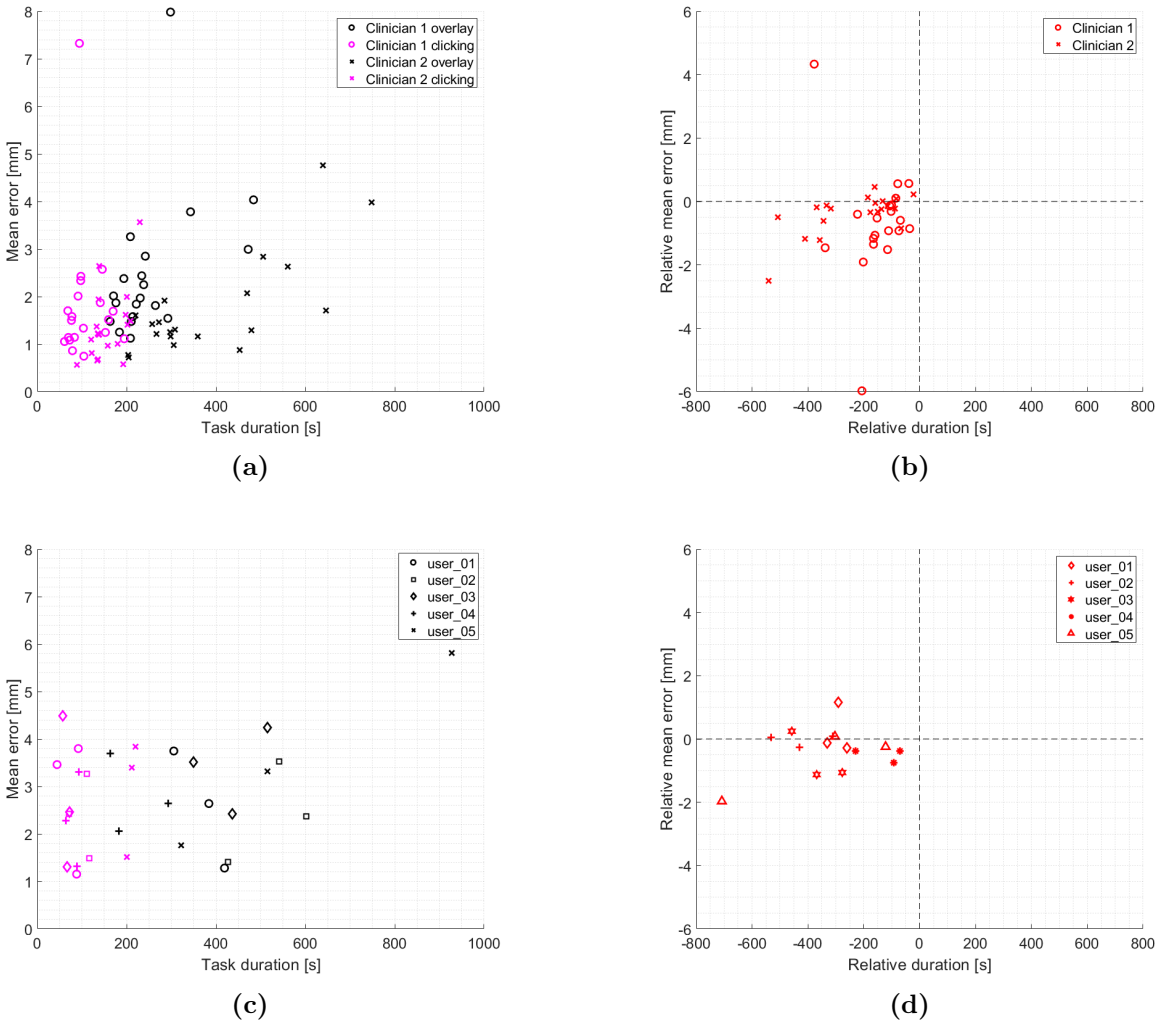

Figure 3.5: **(a)** μ_D versus duration of the task for two clinicians, for the semi-automatic (magenta) and manual (black) tasks. The third clinician was excluded because of erroneously high duration measurements. For the semi-automatic task, a relation between error and duration seems to exist; more time is spent on harder patients, but without giving a better result. **(b)** The same data, but now the manual task is subtracted from the semi-automatic task, giving the relative μ_D and duration. **(c)** Analogous to (a), μ_D versus duration of the task for the five non-clinicians, for the semi-automatic (magenta) and manual (black) tasks. **(d)** The same data, but now the manual task is subtracted from the semi-automatic task, giving the relative μ_Ds and duration. Here, the accuracy seems to be approximately the same between manual and semi-automatic.

3.3.2 Effect of collinearity and point spread

In addition to the error and duration data, the choice of control points for the clinicians is investigated with the degree of collinearity of the three points as well as the spreading out of the control points measured by the size of the triangle that is formed by the control points. Figure 3.6 summarizes that data. A high degree of collinearity of the points seems to allow for a higher μ_D (but it is possible to have a high collinearity and yet a low error). Statistically, there's a significant ($p = 0.000$) correlation between collinearity and μ_D with a Pearson correlation coefficient of $\rho = 0.32$, which fits with the idea that collinearity can introduce error.

For the area of the triangle no significant correlation exists ($\rho = -0.09, p = 0.33$), but some of the tasks with the highest μ_D do seem to have a small area.

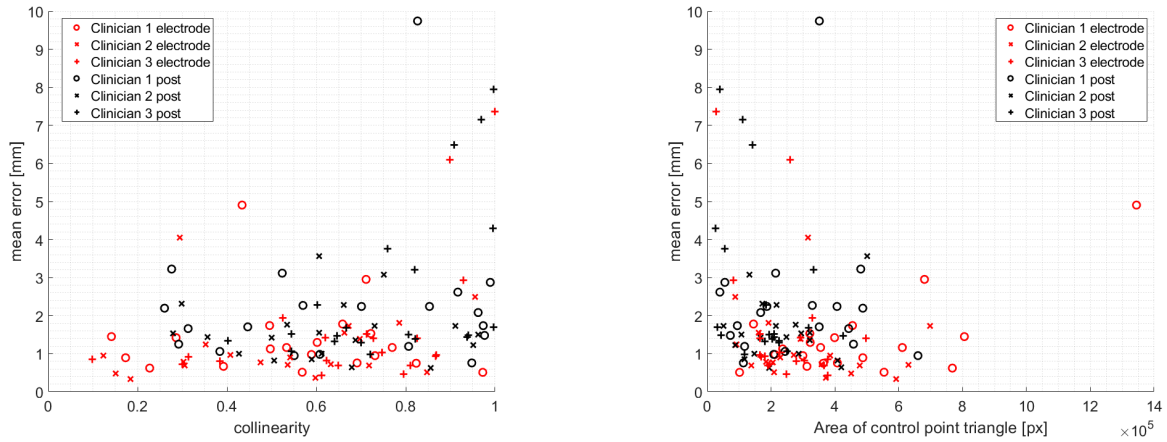

(a) **(b)**

Figure 3.6: (a) Collinearity of the chosen control point sets plotted against the μ_D. The registration tasks with the six highest μ_D all have a collinearity measure of 0.8 or higher. There is a significant ($p = 0.000$) correlation between collinearity and μ_D (Pearson correlation, $\rho = 0.32$). Furthermore, the variance in the μ_D seems to increase with collinearity. (b) The area of the triangle formed by the control points in pixels, set out against the μ_D of the task in mm. The two tasks by clinician 3 with high collinearity show up here as tasks with a low area.

3.3.3 Registration by non-clinicians

The non-clinicians performed the semi-automatic and manual tasks for patients 2, 4 and 6, and in Table 3.2, the mean μ_D, duration and cost metrics over those three patients for all non-clinicians was compared with the clinician tasks for those three patients. Because only the data for patients 2, 4 and 6 was used, the numbers for clinicians are different from the numbers in Table 3.1.

With three patients, adequate statistical testing cannot be done, but it can be seen that for the manual task clinicians and non-clinicians are comparable in accuracy, but clinicians are faster. For the semi-automatic task, the non-clinicians are slightly more accurate and faster, showing that the semi-automatic task is highly intuitive.

Table 3.2: Mean μ_D in millimeters and pixels and duration of tasks in seconds for three patients (EP_02, EP_04 and EP_06), compared between the clinician and the non-clinician group.

		clinicians	**non-clinicians**
Manual	μ_D [mm]	2.7 ± 1.5	3.0 ± 1.7
	μ_D [px]	62.1 ± 33.1	33.8 ± 43.6
	duration [s]	380.9 ± 187.1	425.7 ± 187.3
Semi-automatic	μ_D [mm]	3.1 ± 2.4	2.6 ± 1.3
	μ_D [px]	70.9 ± 51.9	30.1 ± 37.0
	duration [s]	129.0 ± 54.8	106.6 ± 57.2

3.4 Discussion

In this substudy, we compared a manual and semi-automatic way of coregistering corticography photographs by clinicians and non-clinicians, on a set of 20 acute ECoG patients for whom a set of three images (start of surgery, electrode grid position and resection) was available.

The semi-automatic method is superior to the manual overlay method because the duration is much lower, although there is no significant increase in accuracy. It's therefore time efficient whilst maintaining accuracy. The fact that non-clinicians also attained a low error rate and low duration with the semi-automatic task, means that the method can be mastered easily and that it's highly intuitive. Furthermore, the semi-automatic method was described by the clinicians using it as being less cumbersome.

Our results match with those of Dalal et al.[64], giving a mean error of 2.7 ± 1.5 mm. This is a little higher than their error of 2.0 ± 1.0 mm, which could be explained by the fact that we only choose three control points, and we average over data of 20 patients whereas Dalal only uses one of the patients to compute this performance measure. Furthermore, all the photographs in the study of Dalal et al. are of good quality; ours vary more in quality and are therefore a more realistic metric.

In terms of control point positioning, collinearity is positively correlated with error and spread of control points is negatively correlated. Choosing non-collinear, spread out control points is therefore recommended. Because of the inability of the algorithm to cope with non-linearity, it is furthermore recommended to place control points close to the area of interest (e.g. the resection or electrode grid).

In conclusion, this semi-automatic method of image coregistration is ready for use in the research environment, provided that control points are chosen by the user to be not too collinear and spread out. An implementation of this method is already being used in the UMC by researchers to aid with electrode classification.

3.4.1 Limitations

Handling nonlinear deformations

It can be seen that tasks for certain patients, the μ_D per patient is high for all three clinicians, for instance in patients 2 and 5, in the $I_{el} - I_{pre}$ registration. For patient 5 it's less clear why that is the case, but patient 2 is challenging because the I_{pre} picture is from a significantly

different angle than I_{el} and I_{post}, giving rise to non-linear effects that can't be solved with a linear algorithm.

There are two main sources of non-linearity in cortex photographs: perspective changes and brain shift. Perspective changes are non-linear because the brain surface is curved; if it were a flat twodimensional plane the perspective change could be accounted for. To tackle this form of nonlinearity, one could either use the knowledge of the curvature of the brain to model the nonlinearity (for instance when one has an MRI which is linked to the system taking the pictures), or let the camera remain stationary.

Brain shift is a notably harder problem to solve; this is the actual physical deformation of the brain due to manipulation by the surgeon, resection, loss of liquor and swelling. In the case of brain shift, the nonlinearity cannot be accounted for with the brain model and the camera movement. Nonlinear ways of image registration exist, both with feature detection (interpolating between the matched features) and with intensity-based algorithms such as Demon's algorithm[80].

A linear solution to the non-linear problem is to choose the control points close to the region of interest; the non-linear deformation will be smaller close to the control points. This method could be further investigated in later validation studies of the semi-automatic algorithm by computing a weighted $\mu_{D,w}$, where the errors close to the resection or electrode grid are weighted more heavily than those far from it.

Manual overlay as a model for workflow

In this study, the current workflow of comparing and overlaying corticography photographs was approximated by a manual overlay task using an image processing program (GIMP). However, workflows in the UMC vary from person to person in the UMC; some perform the side-by-side analysis, some do the manual overlaying (with or without added nonlinear deformation), and some draw the vascular structure and use that as an overlay technique. The manual method described in this study therefore does not fully represent the various methods that are being used, but it is a valid approximation.

3.4.2 Future research

Fully automatic image registration

If a fully automated image registration system could be implemented, this would open up possibilities to also intraoperatively determine the electrode positions for acute corticography and integrate data directly with the neuronavigation and the MRI. A fully automated system would use feature detection algorithms to automatically detect control points that match between pairs of images, and would then do the transformation automatically.

A preliminary investigation into this possibility has been done and is reported in Appendix F.

Automated electrode localization

A next step towards easier and more efficient linking of data with the anatomy would be automated detection of the electrodes in the image with template matching. This has already

successfully been done in 3D space with CT data[55, 56, 78], but in 2D, the perspectival distortions of the electrode disks create an additional challenge for the matching. Furthermore, photographs are subject to other forms of noise such as specular reflections, different lighting conditions, and obstructions from view by blood, water and electrode leads.

To be able to reliably locate electrodes automatically from photographs, an algorithm implementation needs to be found that is robust against such distortions.

Chapter 4

General conclusion

This thesis set out to guide the neurosurgeon by better informing him or her where the pathological tissue is by way of network biomarkers, and subsequently communicating this in a precise way by helping to link the position of the electrodes with the anatomy.

In chapter 2, network analysis was done on interictal chronic ECoG data in sleep for two epilepsy patients to answer the following research questions:

1. (a) Is there a significant difference between **resected and non-resected** electrodes in terms of out-strength, Betweenness Centrality and PageRank Centrality in chronic ECoG?

   (b) Is there a significant difference between **SOZ and non-SOZ electrodes** in terms of out-strength, Betweenness Centrality and PageRank Centrality in chronic ECoG?

In electrodes situated on tissue that was later resected, there is a significant increase in PageRank Centrality in the gamma band for both patients. For one of the patients, there's also a significant increase in out-strength in the gamma band, and for the other a significant increase in PageRank in the beta and ripple bands. For the seizure onset zone, out-strength in the gamma band and PageRank in the beta and gamma bands showed significant increase in both patients.

These results suggest that hubs and drivers are present in both seizure onset zone and resected tissue, and that it is possible to detect these hubs with functional network measures. Because there are also hubs outside of the resection and SOZ, a bigger cohort of patients is needed to help differentiate physiological from pathological hubs. Subsequently, in a later stage, clinical randomized control trials employing resection areas informed by these pathological hubs may give conclusive evidence of the (in)efficacy of this method in attaining seizure freedom for the patient.

In chapter 3, a semi-automatic method to link electrophysiological data to an anatomical location for acute ECoG is validated by answering the following research question:

2. Is semi-automatic image registration of acute corticography photographs an improvement with respect to manual registration in terms of accuracy and duration?

We concluded that this semi-automatic image registration is indeed an improvement; it is a valuable tool to increase efficiency and ease of use for image registration in the research environment, and is also already being used in that context. With more validation, it could potentially also be rolled out in clinical practice.

In conclusion, the combination of easier electrode localization and more insight into pathological tissue is a small step towards giving the surgeon the tools to help epilepsy patients attain seizure freedom.

Appendix A

Technical background for network analysis

A.1 Directed Transfer Function

The Directed Transfer Function is one of many functional connectivity measures, and is based on Granger Causality[81], which is based on the assumption that if two signals are highly correlated with some time lag, it follows that the later signal can reasonably be *assumed* to be caused by the earlier signal (assumed, not proven). The later signal is said to be *Granger-caused* by the earlier signal.

This concept can be used to quantify functional connectivity by fitting a multivariate autoregressive (MVAR) model to the data. Multivariate because one model fits multiple channels at once, and autoregressive because it also looks at time instances in the past, also in its own signal.

For instance, when computing the Directed Transfer Function of an epoch $\mathbf{x}$, where $\mathbf{x}$ is a matrix with m rows, corresponding to the ECoG channels, and N columns, corresponding to the number of samples, the multivariate autoregressive model is[82]:

$$\mathbf{x_i} = \mathbf{w} + \sum_{l=1}^{p} \mathbf{A_l x_{i-l}} + \boldsymbol{\varepsilon_i} \tag{A.1}$$

Here, $\mathbf{x_i}$ is the vector of values for all channels for sample i, $\mathbf{w}$ is a vector of constants for each channel, $\boldsymbol{\varepsilon_i}$ is noise computed with a covariance matrix $\boldsymbol{C}$ and $\mathbf{A}$ is an $m \times m \times p$ matrix of coefficients, weighing the influence of each channel at each timestep until the model order p. The model order therefore effectively determines how far this connectivity measure can "look back".

The `ARfit` MATLAB package computes the unknown parameters when the user inputs the epoch $\mathbf{x_i}$ and minimum and maximum model orders p_{min} and p_{max}. It does this with a stepwise least squares estimate as described by Neumaier et al.[83]. The to be computed parameters are the appropriate model order $\mathbf{p}$ (determined with the Schwarz Bayesian Criterion[70]), the vector $\mathbf{w}$, the covariance matrix $\mathbf{C}$ that informs the noise term $\boldsymbol{\varepsilon}$, and most importantly, the matrix of coefficients $\mathbf{A}$.

When all these model parameters are computed, the matrix of coefficients can be plugged into the following equation to get the transfer function matrix:

$$\hat{H}(z) = \left(\sum_{j=0}^{p} \hat{A}_j z^{-j} \right)^{-1} \tag{A.2}$$

The Directed Transfer Function (γ_{ij}) is then given by the following equation:

$$\gamma_{ij}^2(f) = \frac{|H_{ij}(f)|^2}{\sum_{m=1}^{k} |H_{im}(f)|^2} \tag{A.3}$$

Here, i is the row index of the connectivity matrix and is the *sink*, and j is the column index and represents the *source*. Each value of the matrix is the connectivity from source to sink, so the second row, fourth column is the connectivity from the fourth to the second channel. In the denominator of this equation, it can be seen that DTF normalizes over the *sources*; all of the rows of $\boldsymbol{\gamma}(f)$ sum up to one. When we sum the columns, however, we get the *out-strength* as will be described later in this appendix.

The DTF $\boldsymbol{\gamma}(f)$ is a function of frequency f; the `ARfit` package outputs an $m \times m \times F$ matrix where F is the number of frequency bins (with a default frequency bin size of 1 Hz). The DTF in a certain frequency band can then be obtained by simply averaging this connectivity matrix over those frequencies.

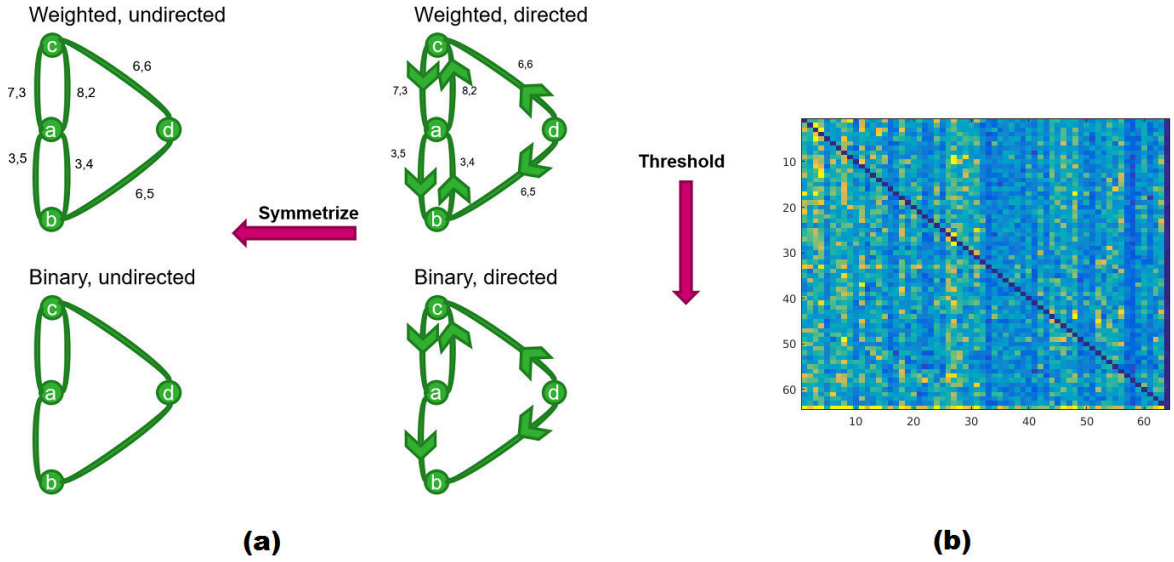

Figure A.1: a: Types of networks. b: Example of a connectivity matrix computed with DTF. Here, the diagonal is set to zero after the DTF has been computed. In this particular example, the networks don't coincide with the connectivity matrix, but in essence they are interchangeable; a network is just another way of displaying a connectivity matrix.

A.2 Network types

With the connectivity matrix as a basis, one can construct a network. In the case of an ECoG recording, the electrodes will function as nodes and the connectivity between the signals on those electrodes are the edges.

Multiple ways of constructing these networks exist.[29] See Figure A.1a for four basic types of networks.

Networks can be **weighted** or **binary**: in a weighted network the connections between all the vertices are present but they have a "weight" or connection strength as determined by the values of the connectivity matrix. A binary network, on the other hand, is thresholded at a certain connectivity strength; pairs of nodes exhibiting at least that connectivity strength will be connected with an edge and others will not.

Networks can be **directed** or **undirected**. In a directed network, the connectivity from node A to B might not be the same as from B to A. When using the Directed Transfer Function, there might be differences in directionality (exhibited by asymmetry of the connectivity matrix). An undirected network, on the other hand, has the same weights in each direction. A directed network can be turned into an undirected network by symmetrizing; this can be done by adding the transpose of the connectivity matrix to the matrix itself and dividing by two.

The DTF connectivity matrix is itself already a weighted, directed network.

A.3 Local network measures

For a more detailed explanation of network measures, we will look at a network generated from data in the Dutch railway system (NS).

Table A.1 shows the number of trains that were in service on Sunday, September 23rd between a number of cities. This is an example of connectivity data between these cities, and is analogous to the result of the computation of the Directed Transfer Function between electrodes.

Table A.1: The direct trains that were in service from each of eight cities to each other city. These trains were tallied on the 23rd of September using the NS Reisplanner. If a train had a direct connection between the two cities, it was counted, even if it also crossed another of these cities inbetween. The unabbreviated city names in order are Amsterdam, Amersfoort, Den Haag, Utrecht, Rotterdam, Nijmegen, Enschede and Woerden.

↓ to →from	**A'dam**	**Amsft**	**DH**	**Ut**	**Rdam**	**Nmgn**	**Ens**	**Wrd**
A'dam	0	72	38	102	150	34	0	33
Amsft	68	0	33	103	32	0	34	0
DH	35	33	0	48	57	0	16	23
Ut	105	71	46	0	59	60	16	70
Rdam	150	34	60	59	0	0	0	33
Nmgn	32	0	0	63	0	0	0	0
Ens	0	31	15	16	0	0	0	0
Wrd	33	0	23	69	35	0	0	0

This matrix of data can be also visualised like in Figure A.2:

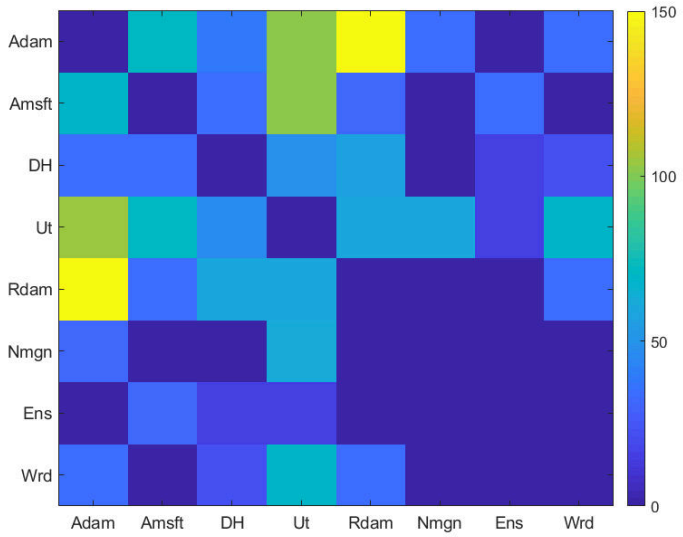

Figure A.2: The connectivity matrix across cities as seen in Table A.1, represented with colors.

This connectivity matrix, where a strong connectivity denotes a lot of trains going in that direction, is itself already a directed, weighted matrix. However, because there is about an equal amount of trains from each destination A to destination B, the matrix is nearly symmetrical/undirected. Asymmetry can for instance be found in the Utrecht - Amersfoort connection, where there are substantially more trains going to Utrecht from Amersfoort (103) than the other way around (71).

Figure A.3 shows the same network as in the connectivity matrix, but the sizes of the nodes are scaled to reflect different network measures. The edge thickness for the connections is the same in each graph and is the total strength of that connection (so the sum of in- and out-strength).

Local network measures are attributes of individual nodes, as opposed to global network measures which are parameters which say something about the network as a whole. In this thesis we will only use local network measures. The local network measures we will be using are *strength*, *Betweenness Centrality* and *PageRank Centrality*.

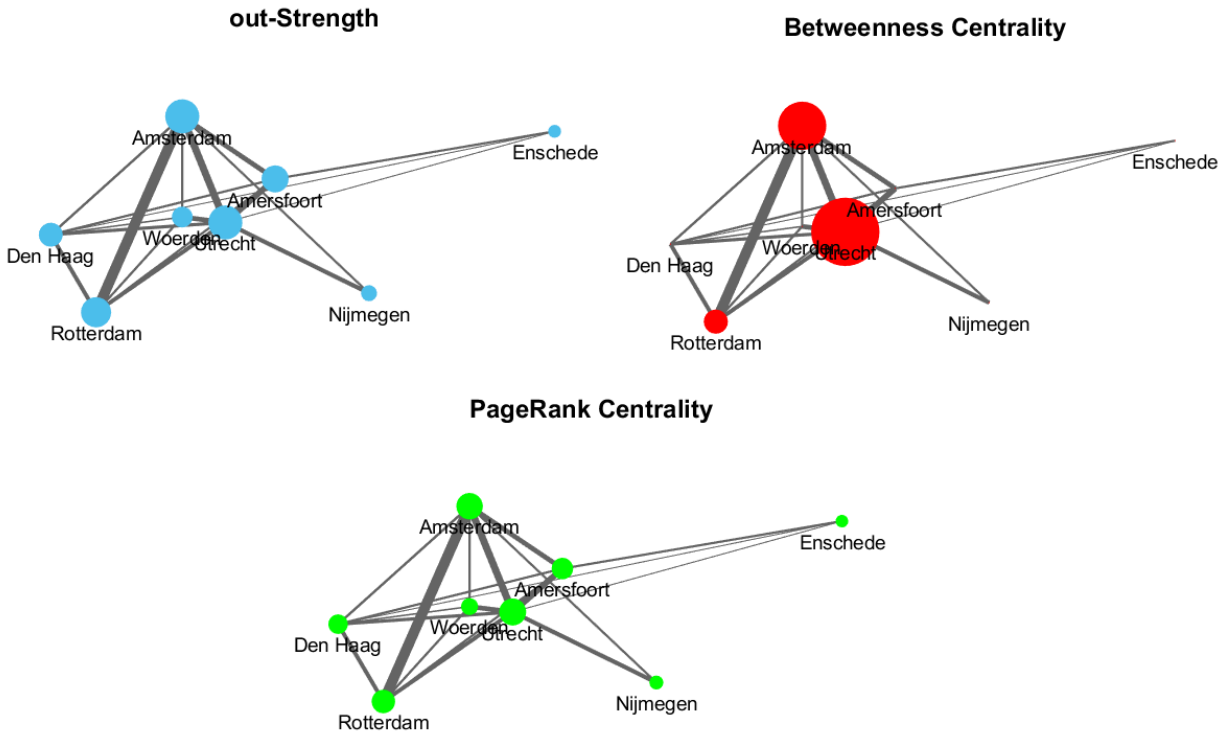

Figure A.3: Examples of three network measures computed on data for the number of direct train connections between Dutch cities on Sunday, September 23rd. The size of each node reflects the relative value of the network measure, normalized within that graph. The edges are proportional to the total strength of the connection. Notable is a high Betweenness Centrality for Utrecht which makes sense since it is an important hub in the train network. Instructive is the relative change of Utrecht with respect to Amsterdam when going from out-strength to BC.

A.3.1 Strength

Strength is simply the sum of all connections of a node in a weighted graph; this could be in-strength (the incoming connections) or out-strength (outgoing connections) or simply total strength. Degree is its counterpart in a binary graph; this is the number of connections to or from a node.

Strength and degree, respectively, are formalized by these expressions:

$$k_i^w = \sum_{j \in N} w_{ij} \tag{A.4}$$

$$k_i = \sum_{j \in N} a_{ij} \tag{A.5}$$

with i and j being node indices (in a directed network, the flow goes from node i to j). k_i^w is strength or weighted degree and k_i is degree. a_{ij} signifies the connection between node i and j and has a value of 1 when a connection is present, and 0 when it is absent.

In-strength and out-strength can be easily computed with a connectivity matrix such as the one in Figure A.2; the in-strength is simply summing over the columns (so in the direction of the rows), so that each row or sink has an in-strength value. Out-strength, similarly, is computed by summing over the rows. The out-strength of for instance Amsterdam can be computed by summing all of the trains coming from Amsterdam to each of our other cities, which is $68 + 35 + 105 + 150 + 32 + 33 = 423$ trains. Because Amsterdam has the highest out-strength, it could be said to be the driver of this network.

An important sidenote is that, with DTF, the values are normalized over the in-strength, so the sum over the columns is by definition 1, except when you remove the diagonals first. If the diagonals are removed, then the in-strength measures therefore become 1 minus the diagonals, which are the self-connections.

A.3.2 Betweenness Centrality

Betweenness Centrality (BC) is a measure of the proportion of shortest paths between all other nodes that pass through the node of interest[19]. It is expressed mathematically by:

$$BC_i = \frac{1}{(n-1)(n-2)} \sum_{h,j \in N h \neq j, h \neq i, j \neq i} \frac{\rho_{hj}^{(i)}}{\rho_{hj}} \tag{A.6}$$

where ρ_{hj} is the shortest path between node h and j and $\rho_{hj}^{(i)}$ is the shortest path between h and j that goes through node i [29].

If we look at our example network of cities in Figure A.3, this principle can be seen in action. For instance, Enschede has a Betweenness Centrality of zero, because it is never a shortest path between any other two cities. However, the topographically layout of the graph might be misleading because the definition of a short path is a high value of the connectivity matrix; Amsterdam - Rotterdam could therefore be said to be the shortest path in the network.

When computing the Betweenness Centrality of Enschede for instance, one would iterate over all different pairs of other cities and add one to the measure if a shortest path goes through Enschede. For each pair, however, this shortest path does not go through Enschede[1].

BC can be high even if a node has low total strength or degree, because if a certain node connects two clusters, a lot of shortest paths will be routed through that node. Nodes with high BC can therefore be interpreted as *connecting* hubs, typically inbetween clusters.

[1] As was painfully obvious during my time as a student there...

When using BC for brain data, implicitly a "shortest path" information routing assumption is made. This may not be an appropriate assumption for the brain[19] because to be able to take the shortest path, a firing population of neurons has to have knowledge of the topology of the network somehow.

In this example of trains between cities, the Betweenness Centrality was computed on the *elementwise* inverted matrix; that is, the matrix for the shortest path **S** was constructed by subtracting each element of the connectivity matrix **C** from the maximum of **C**:

$$S_{ij} = max(\mathbf{C}) - C_{ij} \tag{A.7}$$

This was done because inverting the matrix produced counterintuitive results (Enschede having a nonzero BC for instance).

A.3.3 PageRank Centrality

PageRank Centrality (PC) is a measure which recursively also takes into account the centrality of nodes adjacent to the node in question to compute its centrality[19]. In other words, a node is important when it is linked to by other important nodes.

Mathematically, PageRank Centrality can be expressed as follows[19]:

$$PC = D(D - \alpha A)^{-1}\mathbf{1} \tag{A.8}$$

where D is a diagonal matrix of node out-degrees where $D_{ii} - max(k_i^{out}, 1)$ and k_i^{out} is the out-degree **1** is a column vector of ones, A is the connectivity matrix and α is a damping factor, usually set to 0.85. This measure was used for Google' page ranking algorithm[31, 84].

PageRank Centrality can also be computed iteratively. On the first iteration, the PageRank of all the nodes is equal (1/N where N is the amount of nodes)[85].

$$PC(p_i; 0) = \frac{1}{N} \tag{A.9}$$

For each timestep, the PageRank of each node gets divided over all the other nodes that it is connected to, weakened by the damping factor α:

$$PC(p_i; t+1) = \frac{1-\alpha}{N} + \alpha \sum_{p_j \in M(p_i)} \frac{PC(p_j; t)}{L(p_j)} \tag{A.10}$$

In their paper, Page and Brin[84] provided an instructive interpretation of PageRank as the probability that a surfer of the web, that is clicking on links within pages, lands on a certain page.

The damping factor, in the application that Google used it for (ranking search results in order of importance), can be explained as the likelihood that a "web surfer" will get bored of clicking on pages and will be instantiated at a random page to start another clicking session. In neural networks, it could therefore be seen as a sort of extinction of the signal as it propagates through the nodes.

When we look at our train example, the PageRank could be seen as the probability of ending up at a certain station when randomly taking trains from station to station. The damping factor of less than one makes sure that if a node is terminal and no connections come from it, this random traveler will not get stuck but "teleports" to a different node to continue her journey.

Similar to Betweenness Centrality, PageRank also has an underlying assumption about information flow in the network, which is more aligned with how the brain works[19]. Because PageRank is akin to diffusion of information, it fits with a parallel transfer model of information flow, where a firing population of nodes spreads a signal to other nodes in a growing "sphere" of influence.

The damping factor α is set to 0.85 for this study; this is a conventional measure. It has to be lower than the biggest eigenvector of the connectivity matrix and is bounded by 1[19]. If it's higher, the PC will be influenced more by the topology of the network, and if it's lower, centrality measures will be more locally determined and become more similar.

Appendix B

PageRank plots of unresected patients

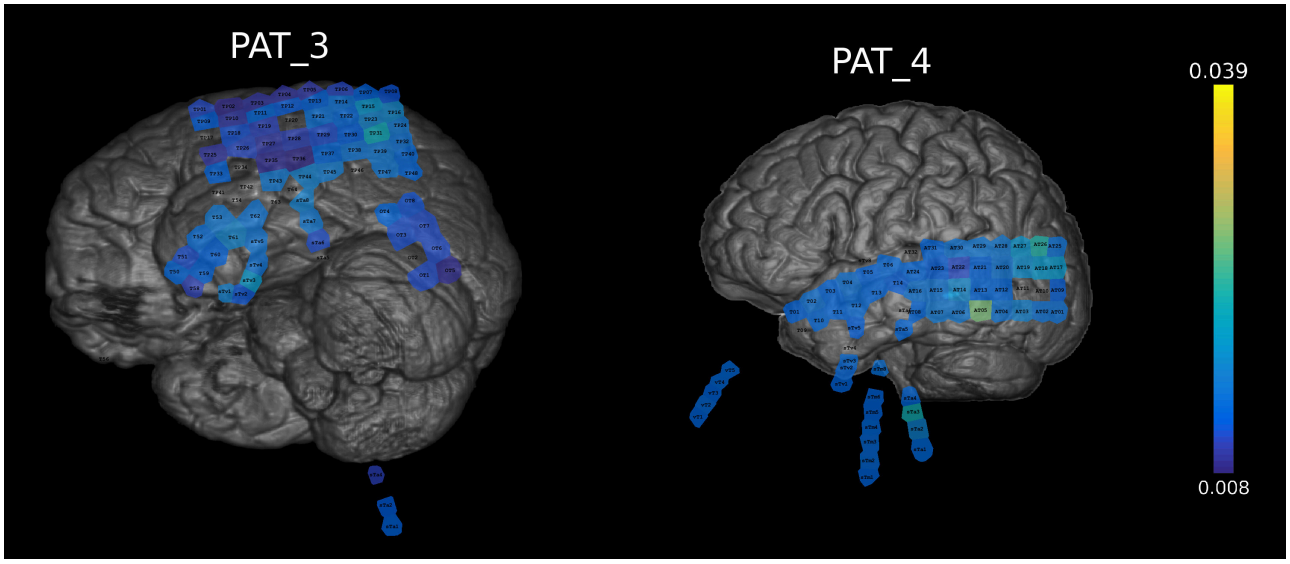

Figure B.1: PageRank Centrality in the ripple band for patient 3 and 4, in the S+ epoch type (sleep with events). Resected area is outlined with red and areas with unknown resection status are outlined with green. In patients 3 and 4 (who are not resected), interestingly, the values of PageRank seem to be continuous and showing peaks, for patient 3 at TP31 and for patient 4 at AT26 and AT05. Within the network disease paradigm, these locations could be of interest to resect.

Appendix C

Box plots for all states

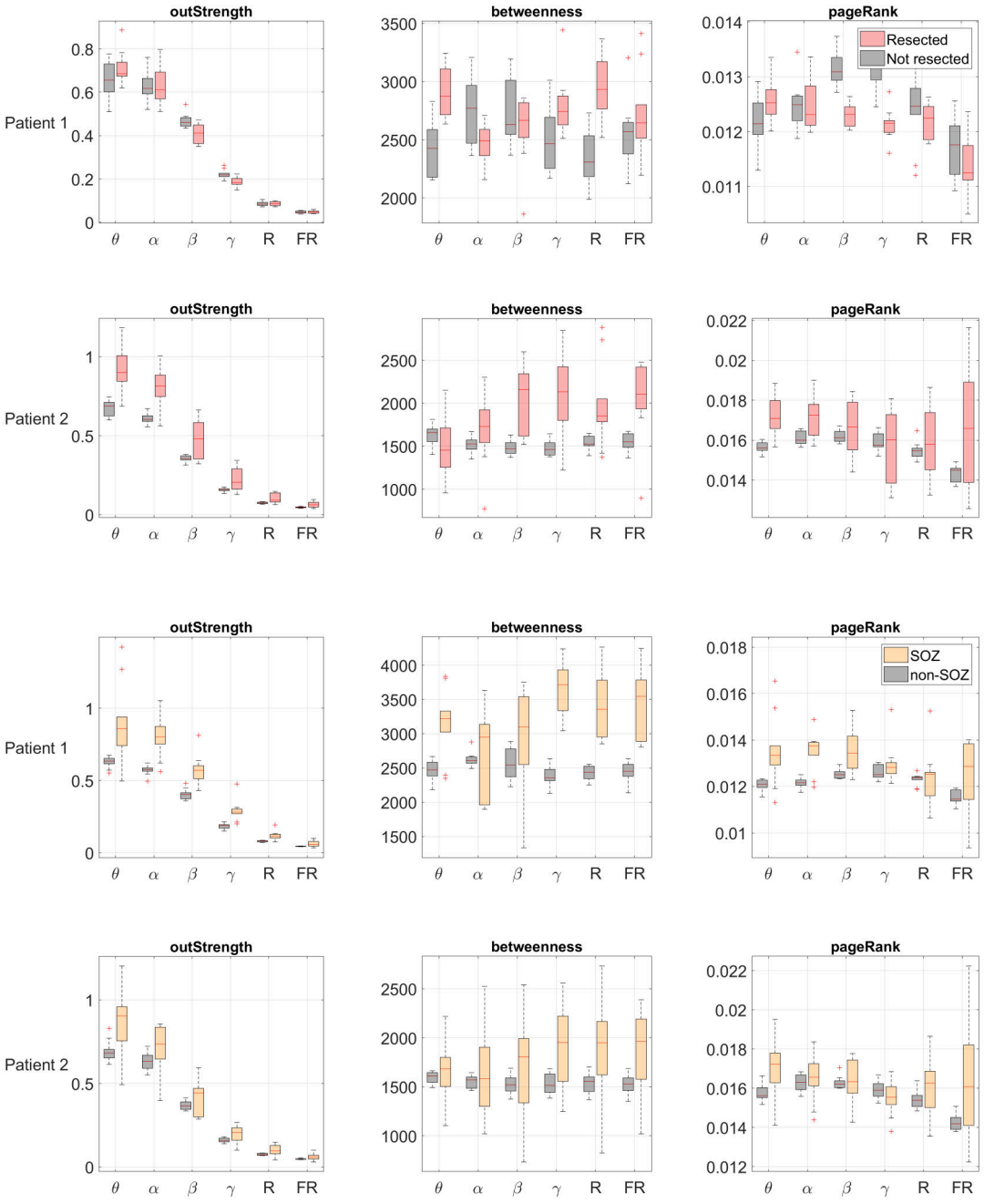

Figure C.1: Boxplot of median network measures of resection versus non-resection channels, and SOZ versus non-SOZ channels, in awake minus events (A-) state. Each box, including its outliers, represents the medians per category in ten separate epochs.

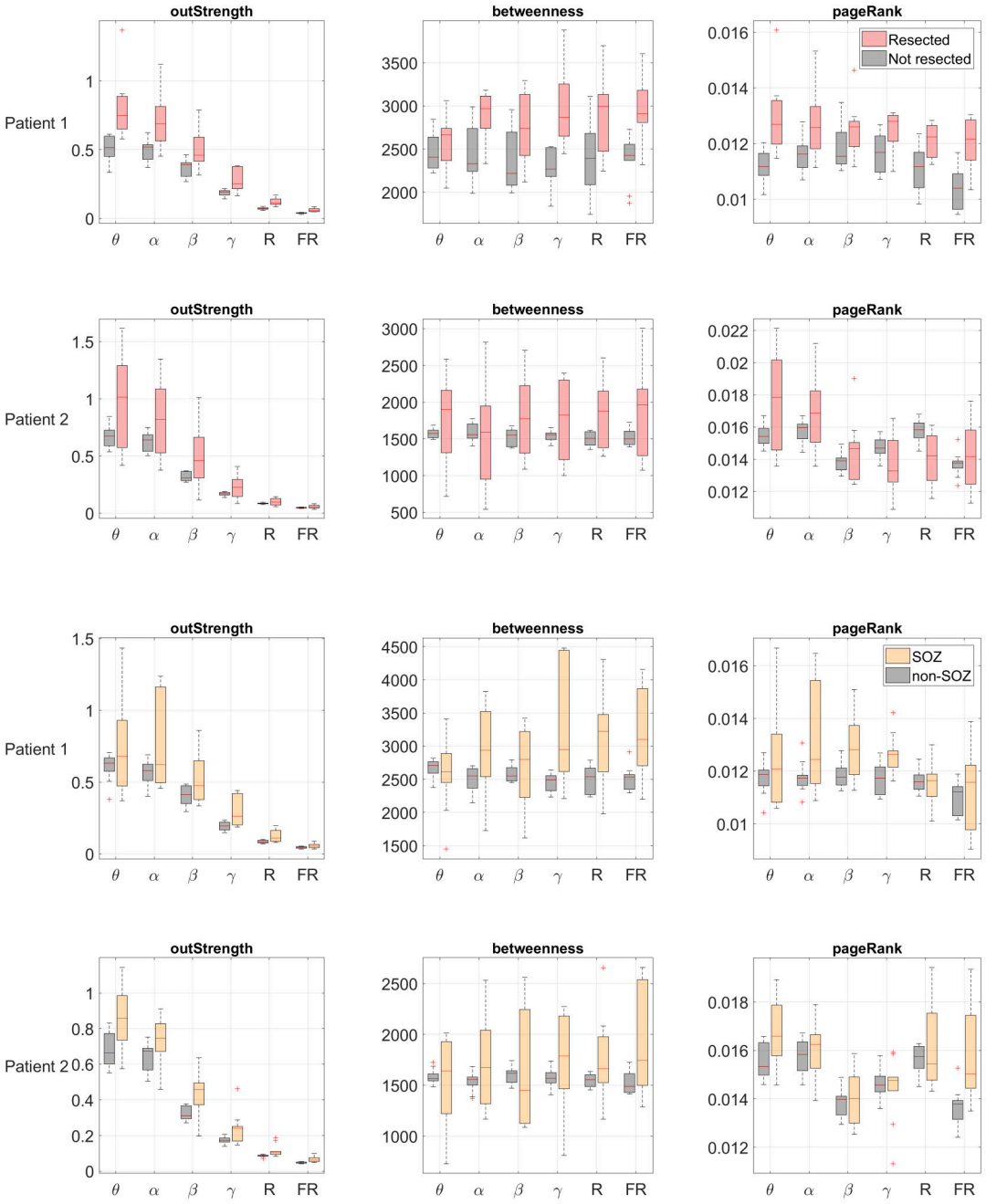

Figure C.2: Boxplot of median network measures of resection versus non-resection channels, and SOZ versus non-SOZ channels, in awake plus events (A+) state. Each box, including its outliers, represents the medians per category in ten separate epochs.

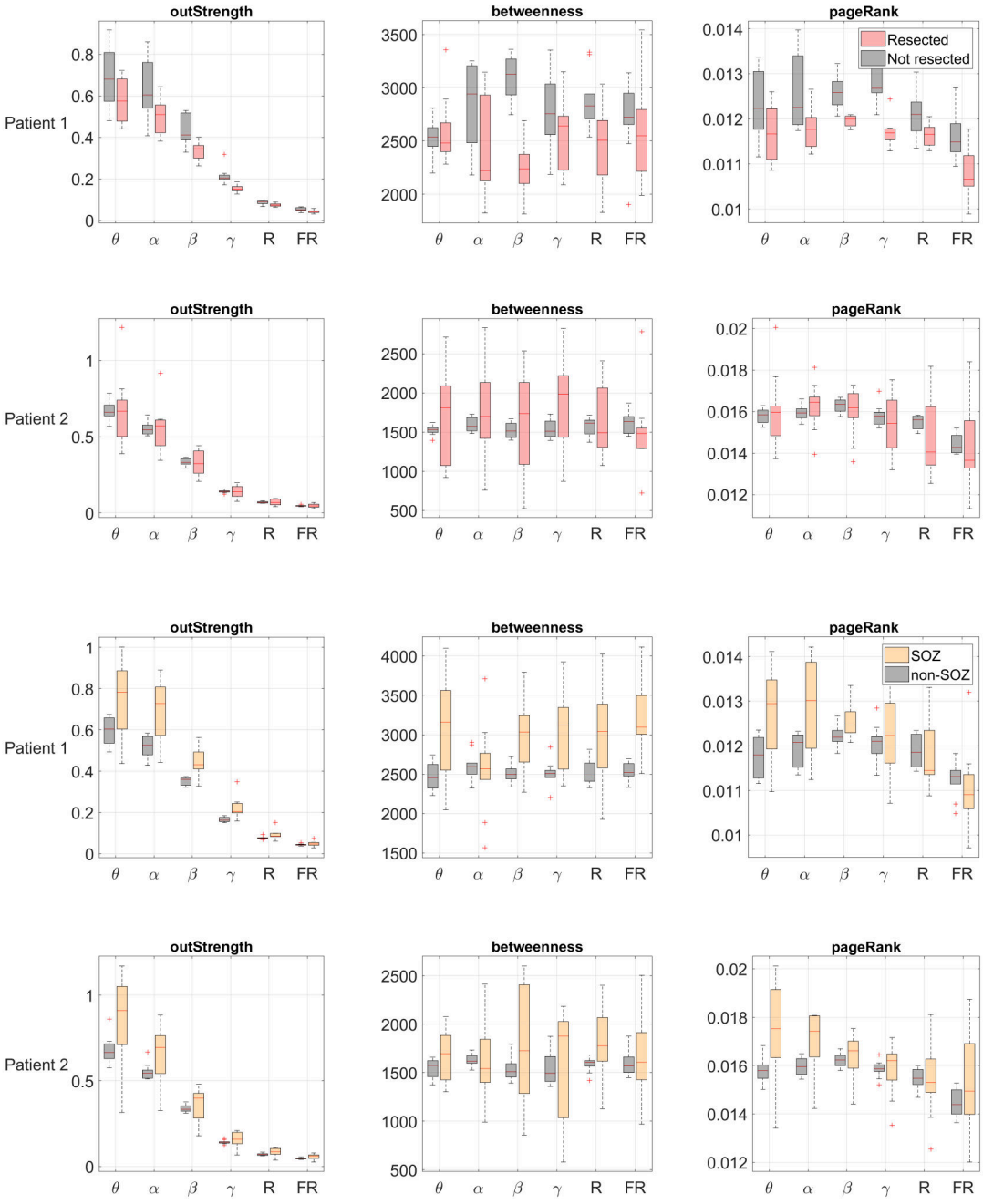

Figure C.3: Boxplot of median network measures of resection versus non-resection channels, and SOZ versus non-SOZ channels, in sleep minus events (S-) state. Each box, including its outliers, represents the medians in ten separate epochs.

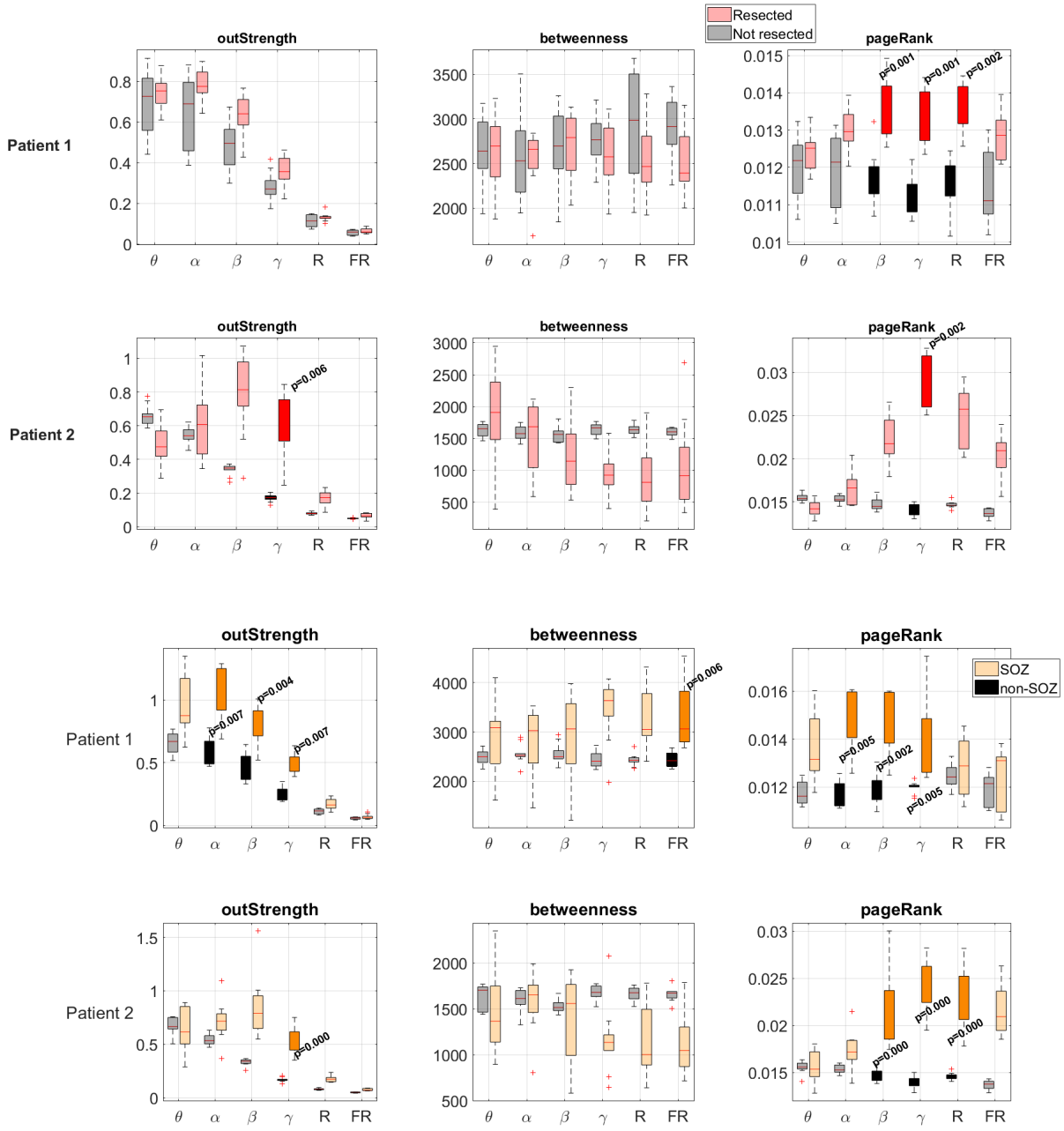

Figure C.4: Boxplot of median network measures of resection versus non-resection channels, and SOZ versus non-SOZ channels, in sleep plus events (S+) state. Each box, including its outliers, represents the medians per category in ten separate epochs. Opaque coloring signifies a significant p-value ($\alpha = 7.5 \times 10^{-3}$) resulting from Wilcoxon ranksum analysis, and therefore a significant difference in the values within the SOZ and outside of it, or within the resection and outside of it. These values are the mean values of the 10 epochs. The significance level was chosen by doing a Benjamini-Hochberg procedure to control the false discovery rate. One of the things that can be seen for patient 2 is significantly increased out-strength in and significantly increased PageRank in the gamma band. Patient 1 had significantly higher PageRank in the resection area for the beta, gamma and ripple bands, although the difference is smaller than for patient 2.

Appendix D

Transformation types

A transformation can be defined as a mapping from one coordinate frame to the other[58]. Let's say ${}^{M}\mathbf{p}$ is a set of three twodimensional control points for the moving image in the following form:

$$ {}^{M}\mathbf{p} = \begin{bmatrix} p_{x1} & p_{x2} & p_{x3} \\ p_{y1} & p_{y2} & p_{y3} \\ 1 & 1 & 1 \end{bmatrix} \tag{D.1} $$

where element p_{x1} is the x-coordinate of the first control point. ${}^{F}\mathbf{p}$ is the set of three control points in the fixed coordinate frame, defined analogously. The addition of the row of ones is done for mathematical reasons, to homogenize the coordinates.

A linear transformation can now be expressed as a 3x3 matrix ${}^{F}\mathbf{T_M}$ which transformed points from F to M when points are multiplied by this matrix. This matrix has the following basic form (notice the 1 for homogenization in the right lower corner):

$$ {}^{F}\mathbf{T_M} = \begin{bmatrix} a & b & c \\ d & e & f \\ g & h & 1 \end{bmatrix} \tag{D.2} $$

The transformation then becomes:

$$ {}^{F}\mathbf{T_M}\,{}^{M}\mathbf{p} = {}^{F}\mathbf{p} \tag{D.3} $$

The control points in both the moving and the fixed frame are known; these are put in by the user. The task for our registration algorithm is then to find this matrix ${}^{F}\mathbf{T_M}$ that transforms the moving points into the coordinate frame of the fixed points with minimal error, which means minimizing this sum:

$$ \sum_{n=1}^{N} || \, {}^{F}\mathbf{T_M}\,{}^{M}\mathbf{p} - {}^{F}\mathbf{p}||^2 \tag{D.4} $$

A solution to this is to perform a Least Squares Estimation, which is basically a way of rewriting Equation D.3 to get all of the known variables to the right side of the equation:

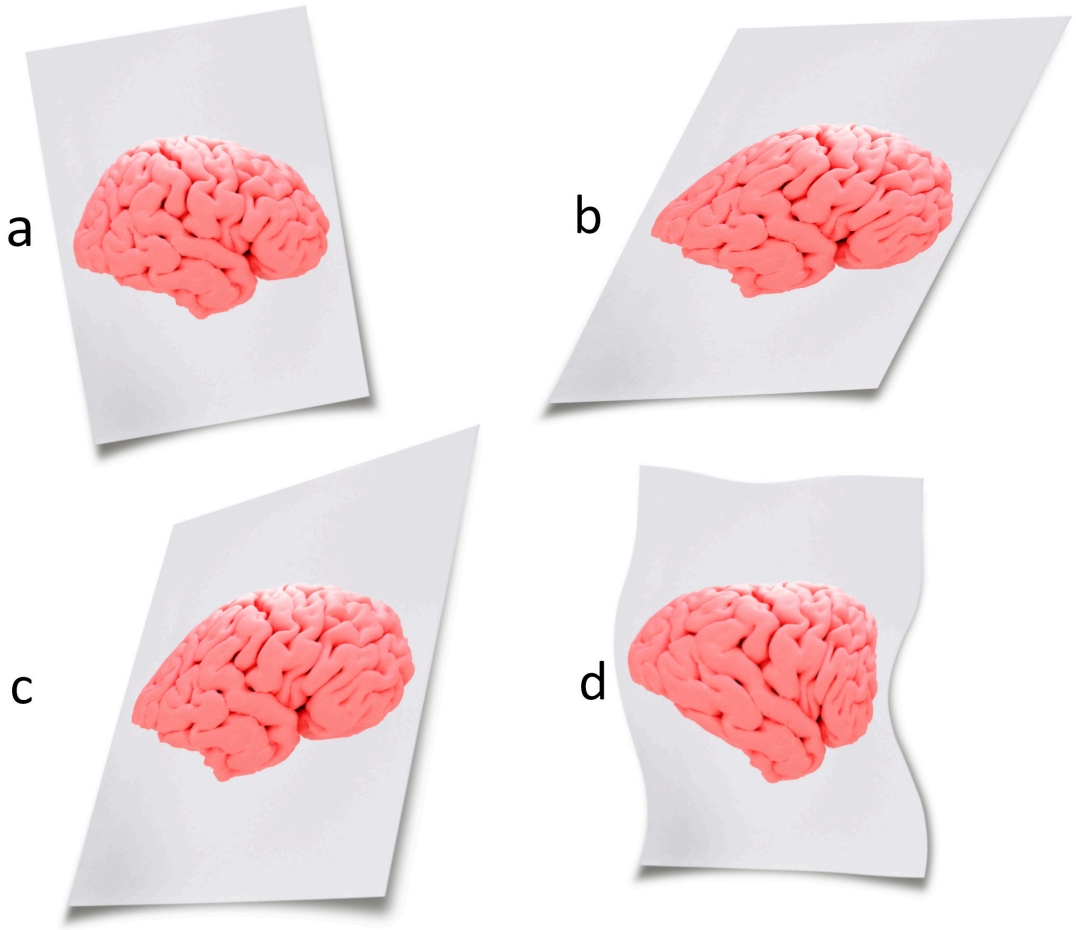

Figure D.1: Four transformation types. **a**: selfsimilar transformation; only rotation, translation and scaling are allowed. **b**: affine transformation; shearing is additionally allowed. **c**: projective, a projective transformation is additionally allowed. A through c are linear transformations. **d**: non-rigid or non-linear transformation. Figure modeled after Fig 5 in [58].

$$ {}^{F}\mathbf{T}_{\mathbf{M}}\,{}^{M}\mathbf{p} = {}^{F}\mathbf{p} \tag{D.5} $$

$$ {}^{F}\mathbf{T}_{\mathbf{M}}\,{}^{M}\mathbf{p}\,{}^{M}\mathbf{p}^{T} = {}^{F}\mathbf{p}\,{}^{M}\mathbf{p}^{T} \tag{D.6} $$

$$ {}^{F}\hat{\mathbf{T}}_{\mathbf{M}} = {}^{F}\mathbf{p}\,{}^{M}\mathbf{p}^{T}({}^{M}\mathbf{p}\,{}^{M}\mathbf{p}^{T})^{-1} \tag{D.7} $$

The degrees of freedom in ${}^{F}\hat{\mathbf{T}}_{\mathbf{M}}$ (and so the variables a through g that are varied) depend on the transformation type.

Translation is represented by this transformation matrix:

$$ {}^{F}\mathbf{T}_{\mathbf{M}} = \begin{bmatrix} 0 & 0 & 0 \\ 0 & 0 & 0 \\ t_x & t_y & 1 \end{bmatrix} \tag{D.8} $$

where t_x is translation in the x direction and t_y in the y direction.

Rotation is represented as follows, with θ the rotation angle:

$$ {}^{F}\mathbf{T}_{\mathbf{M}} = \begin{bmatrix} cos(\theta) & sin(\theta) & 0 \\ -sin(\theta) & cos(\theta) & 0 \\ 0 & 0 & 1 \end{bmatrix} \tag{D.9} $$

Lastly, shearing is controlled by these elements in the matrix:

$$ {}^{F}\mathbf{T}_{\mathbf{M}} = \begin{bmatrix} 1 & sh_y & 0 \\ sh_x & 1 & 0 \\ 0 & 0 & 1 \end{bmatrix} \tag{D.10} $$

Note that the same elements that control rotation also control shearing.

A more complex transformation that incorporates all three of these transformations can be easily computed by just subsequently multiplying the matrices.

Three linear transformation types and one non-linear transformation type are shown in Figure D.1.

A **similarity** transform (Figure D.1a) is a transform that only uses translation, rotation and scaling (no shearing). An affine transform (Figure D.1b) also allows for shearing. Both of these transforms can have nonzero elements in all of the places except the first two elements of the rightmost column:

$$ {}^{F}\mathbf{T}_{\mathbf{M}} = \begin{bmatrix} a & b & 0 \\ d & e & 0 \\ g & h & 1 \end{bmatrix} \tag{D.11} $$

Similarity transforms are therefore subsets of affine transforms (but not the other way around).

A **projective** (Figure D.1c) transform is a transform where all of the elements can be nonzero, as in Equation D.2. Here, variables c and f determine the vanishing point.

Lastly, a non-linear transform as depicted in (Figure D.1d) cannot be captured with a linear transformation matrix; there has to be a more complex mapping function. Non-linear transformations are out of the scope of this appendix.

In the task of coregistering cortex photographs, there's often a non-linear deformation, for instance due to a perspective shift between two camera angles (with the nonlinearity being that objects that are closer to the camera will shift more), and due to the malleability of the brain. This non-linear shift is estimated with a linear affine transformation, and the error made as low as possible with the three control points that are used.

Sources for this section are the course Surgical Navigation Technology at the University of Twente and the MATLAB documentation.

Appendix E

Extra figures and tables for image registration

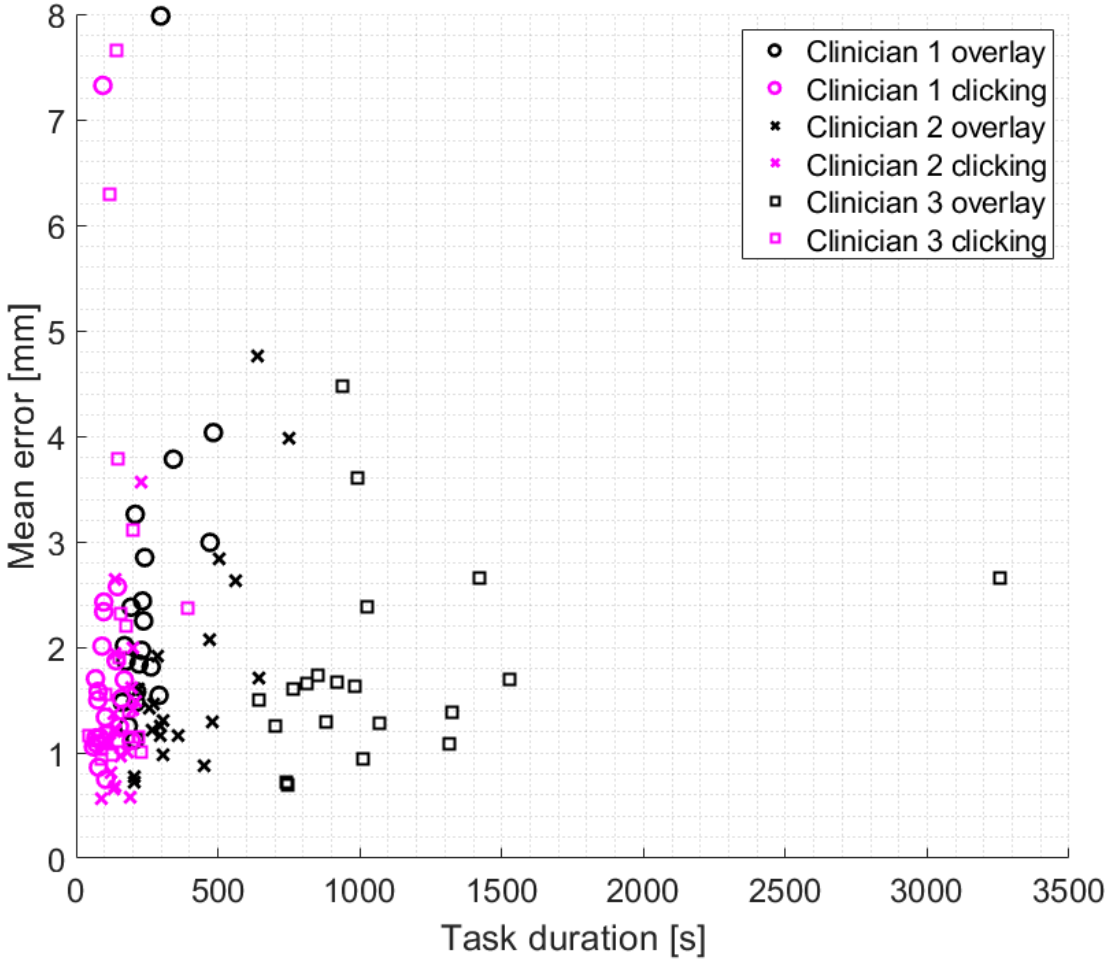

Figure E.1: μ_D versus duration of the task, now including the third clinician, for the clicking (magenta) and overlay (black) tasks. For the clicking task, a relation between error and duration seems to exist; more time is spent on harder patients, but without giving a better result.

Table E.1: μ_D in mm and pixels and duration in seconds for the five non-clinicians for the overlay and clicking tasks, as well as the total mean.

		user 1	**user 2**	**user 3**	**user 4**	**user 5**	**total**
Manual	μ_D [mm]	2.56 ± 1.57	2.44 ± 1.25	3.40 ± 1.68	2.80 ± 1.11	3.63 ± 2.88	2.96 ± 1.75
	μ_D [px]	29.12 ± 38.57	27.75 ± 34.26	38.83 ± 48.37	31.94 ± 37.07	41.22 ± 60.49	33.77 ± 43.58
	duration [s]	370 ± 58	524 ± 89	434 ± 82	213 ± 70	588 ± 310	426 ± 187
Semi-automatic	μ_D [mm]	2.80 ± 1.46	2.39 ± 1.18	2.75 ± 1.63	2.30 ± 1.10	2.92 ± 1.65	2.63 ± 1.34
	μ_D [px]	32.25 ± 40.76	27.30 ± 33.51	31.16 ± 40.18	26.20 ± 31.78	33.43 ± 43.50	30.07 ± 37.00
	duration [s]	75 ± 26	99 ± 25	66 ± 8	82 ± 16	210 ± 10	107 ± 57

Appendix F

Fully automatic algorithm

Fully automated registration algorithms also perform the feature detection and matching steps; the matching features in both images (hereafter called "control points") are automatically detected by the algorithm. There is a variety of feature detection and matching algorithms to choose from, each with their strengths and weaknesses. These algorithms can for instance detect lines or corners, and some are scale and rotationally invariant, enabling detection of rotated features or features on a different scale. Other algorithms don't use features but are *intensity based* and directly use the pixel or voxel intensities to perform the registration. One such algorithm is Thirion's Demon's algorithm (named after Maxwell's Demons)[80] framing image registration as a diffusion problem.

In this preliminary study, we investigate the performance of a number of feature detection algorithms (FAST, BRISK, SURF, MSER, Harris and MinEigen) and subsequent affine transformation on 20 sets of acute corticography photographs.

F.1 Methods

For the fully automated algorithm, the user also selects the pictures and the linear transformation type, and then subsequently lets the algorithm choose the control points. First, the images are preprocessed. The histograms are equalized with the `histeq` MATLAB function which iteratively chooses the transformation T that minimizes this expression:

$$|\mathbf{c_1}(\mathbf{T}(\mathbf{k})) - \mathbf{c_0}(\mathbf{k})| \tag{F.1}$$

where $\mathbf{c_0}$ is the cumulative histogram of the to be registered image I_{moving}, $\mathbf{c_1}$ is the cumulative sum of the histogram of I_{fixed}, and $\mathbf{k}$ are the intensity levels of the histogram.

Subsequently, a conversion to black and white is made where the contrast between the blood vessels and the brain is maximized. This is done by labeling the pixel values of four extra patients (seen as "training data" and with labels ET_01 through ET_04) with the labels "small vessels", "large vessels" and "cortex". Figure F.1c shows the scatter plots of these three tissue types of these four patients in the LAB colour space (lightness (L), green-red (A) and blue-yellow (B) components) For this labeling, the I_{pre} photographs were used only.

The centroids of these pixel clusters of different tissues (C_{sv} for small vessel, C_{lv} for large vessel and C_b for brain tissue or cortex) were averaged over the four patients. To obtain different

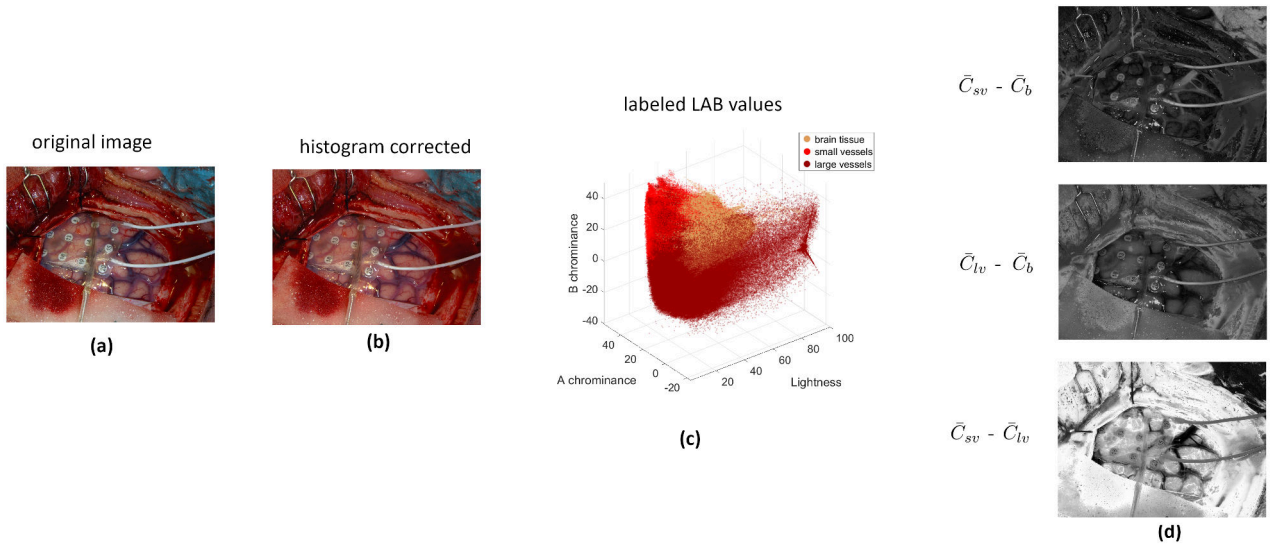

Figure F.1: Preprocessing of the brain images in the fully automatic pipeline. (a) is the raw image, in this case the electrode image for patient ET_03. In (b) the histogram has been equalized with the "pre" photo of this patient. The scatterplot in (c) displays the LAB color values for the three labeled tissue types for the four test patients. In (d), the different mappings to grayscale are shown, from top to bottom using the small vessel to brain centroid axis, the large vessel to brain centroid axis, and the small vessel to large vessel centroid axis to map onto.

grayscale mappings, every pixel value was projected onto one of three vectors; the vector from small vessel to large vessel ($\bar{C}_{sv}$ - $\bar{C}_{lv}$), from small vessel to brain ($\bar{C}_{sv}$ - $\bar{C}_b$) and from large vessel to brain ($\bar{C}_{lv}$ - $\bar{C}_b$). See Figure F.1d for the result of those three mappings.

Eventually, the mapping from small to large vessel was selected, because visually it seemed to give the most feature-rich images for feature detection algorithms.

Subsequently, a number of feature detection algorithms is run on both images of the pair, namely FAST, BRISK, SURF, MSER, Harris and MinEigen.

For each of these detected points, a number of feature descriptors is extracted, so that each combination of feature detection and extraction algorithm is tried. After extraction of the descriptors, these features are matched to find corresponding points. If enough corresponding points are found, a linear transformation is done with the control points. If the method yields a large amount of matches, a nonlinear transformation can be attempted. This is preferable, seeing as the perspective change and potential brain shift are nonlinear phenomena when looking from the vantage point of the camera.

Ultimately, the user checks the goodness-of-fit as done with the manual algorithm, and if need be, selects another linear transformation to try.

F.2 Results

See Tables F.1 and F.2 for all of the μ_D values when running the six algorithms against the 20 preprocessed image sets. Each algorithm was run against the full size, half size and quarter size versions of the images.

FAST and BRISK almost invariably fail to generate an estimated tranformation matrix due to insufficient matched points. The rest (SURF, Harris, MinEigen and MSER) generate estimated transformation matrices and give a result.

In Tables F.1 and F.2, a value above 10 mm μ_D is considered a total mismatch and is printed in red. When looking at the good matches (in black), it is seen that the algorithm that performs best by far is the SURF algorithm on the $I_{el} - I_{pre}$ image pairs, with about half of the image pairs being coregistered well.

It does seem to be influenced by the input image size; for instance EP_12 only has a good coregistration when using the half sized images, and EP_17 has a good coregistration with only the quarter sized images. For the SURF algorithm and the $I_{el} - I_{pre}$ image pair, the full, half and quarter image pairs give a good registration 45%, 60% and 65% of the time (with a good registration being a μ_D below 10 mm).

The mean and standard devation μ_D of only this subset of good registrations is 2.0 ± 1.5 for the full size SURF registration, 1.9 ± 1.1 for half size, and 1.7 ± 1.3 for the quarter size, thereby being approximately as accurate as the clinicians for the overlay and clicking tasks.

See Figure F.2 for the plotted data for the SURF algorithm, and see Figure F.3 for three examples of bad coregistrations, and three examples of good ones.

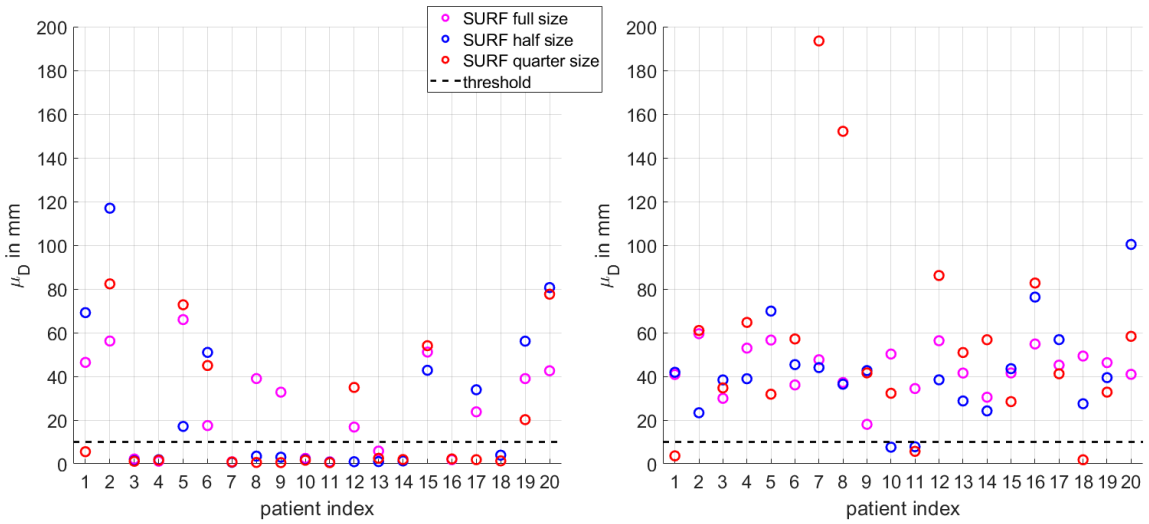

Figure F.2: μ_D in mm for the $I_{el} - I_{pre}$ (left) and $I_{post} - I_{pre}$ (right) image pairs for the SURF algorithm. The threshold of 10 mm to define a successful registration is plotted as a black line. Every image size that the algorithm is applied to is plotted separately. It is seen here that the electrode image registration on the left is done much more successfully than the post image registration on the right.

Discussion

The fully automated algorithm as implemented here does not consistently perform well. Especially the $I_{post} - I_{pre}$ image pair registration seemed to be problematic. Possible reasons are:

- The different lighting conditions due to the neurosurgeon changing the positions of the lamps in the OR. Seeing as the post-resection photograph is made significantly later than the electrode photograph, a change in lighting between those two photographs becomes more likely. Apart from different shades that the brain will get, the specular reflections of the wet brain will also shift and decrease the similarity between photographs.

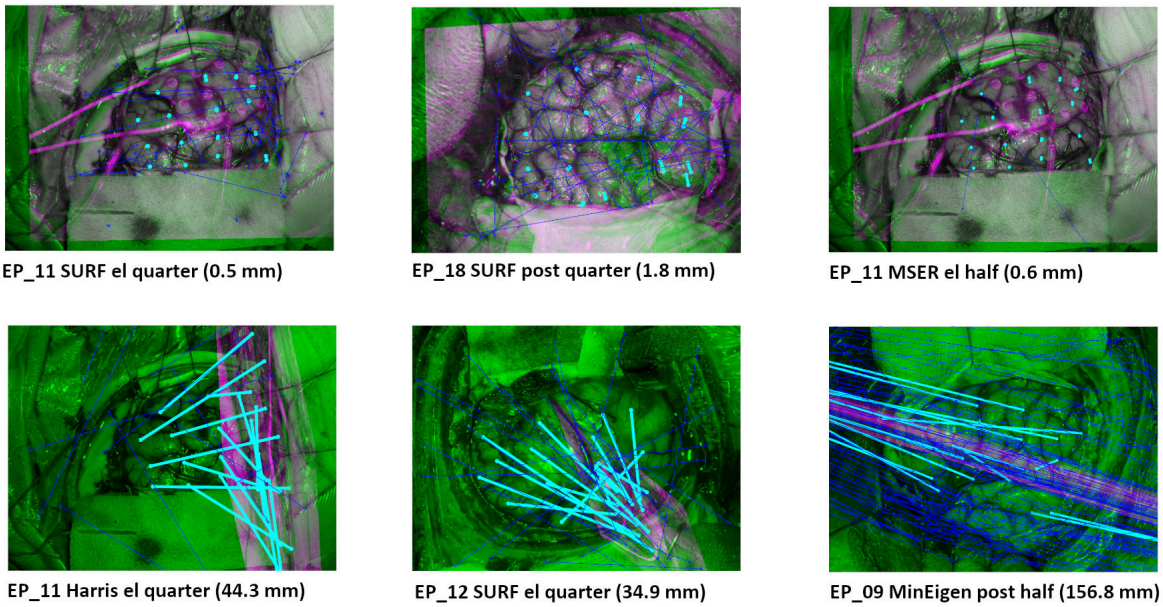

Figure F.3: Examples of good coregistrations (top row) and mismatches (bottom row) of some of the automatic registration algorithms. These are fused images with the green being the I_{pre} image and the purple being either I_{el} or I_{post}. The cyan lines are the 16 ground truth points in both images; the mean length of these lines is used for the μ_D measure. The dark blue crosses and lines are the features that have been matched by the feature detectors. A subset of these features is chosen (the inliers) by the `estimateGeometricTransform` function and the estimated affine transformation is made.

- The vessels often have different amounts of filling; the small arterioles and venules sometimes swell or shrink depending on the amount of blood that is in them. This makes their appearance less consistent across photographs, and therefore makes it harder to match them.
- Sometimes, bleeding causes parts of the brain to change hue, this might be problematic.
- Photographs may have different levels of sharpness; this could also be a problem.

Influence of image scale

Image scale is a factor of influence; care must therefore be taken in choosing what scale to input into the algorithm. The SURF algorithm is has rotational and scale invariance, but up to a certain degree.

A possibility in future research could be to first standardize the sizes of the images; this could potentially increase the matched points.

Grayscale conversion

The grayscale conversion that is used is based on the centroids of the pixel values of the three tissues (large vessels, small vessels, and brain tissue) in the LAB colour space. These pixel values were obtained from the I_pre images. In future research, the I_{el} images could be included in this labeling set to also be able to characterize the colours of the tissue when partly obscured

by the silicone mat of the electrode grid. This might increase the contrast in those areas and facilitate a good match.

Furthermore, this labeling was done in four separate patients. A larger set of patients might help to be able to generalize the conversion to obtain a good contrast in as many patients as possible.

To further help create a contrast between tissues, additional preprocessing such as edge detection could be used to accentuate the vasculature more. Segmentation of the vessels could also be used with subsequent skeletonization to obtain the graph of the vessel network; similar nodes could then be found in the other picture.

Alternatively, a more conventional grayscale conversion could also be used.

Substantial amount of off-brain features

A lot of the matched features in the successful automatic registration were found just beyond the edge of the visible brain, often on the skull, skin or on the surgical cotton pads. Pores in the pads or stubbles on the shaved skin provided the algorithm with interesting features to latch on to.

The problem with this is that it makes the algorithm more susceptible to brain shift; it creates a reference outside the brain which doesn't necessarily move along with it. Furthermore, when one of the cotton pads is moved by the surgeon this further confounds the registration.

In futher research, a way must be devised to emphasize the cortical structures and de-emphasize the surroundings.

Table F.1: For the $I_{el} - I_{pre}$ image pair, these are all values of μ_D for the fully automatic algorithm registration in mm. For each of the algorithms, the images were run through the algorithm in full size, half size and quarter size. A missing value signifies that the algorithm was unable to estimate a transformation matrix due to insufficient matched features. A μ_D above 10 mm is printed as red and considered a total mismatch; μ_D values below that are printed in black and bold.

	FAST			**SURF**			**BRISK**			**Harris**			**MinEigen**			**MSER**		
	full	half	quarter	full	half	quarter	full	half	quarter	full	half	quarter	full	half	quarter	full	half	quarter
EP_01	-	-	-	46.4	69.2	**5.5**	-	-	-	41.3	124.1	47.6	57.6	35.3	19.7	47.9	-	-
EP_02	-	-	-	56.2	117.0	82.3	-	-	-	58.7	74.9	24.8	80.5	65.2	273.0	66.0	69.6	-
EP_03	-	-	-	**2.2**	**1.4**	**1.1**	-	-	-	19.6	**1.5**	14.7	63.2	85.0	39.2	72.6	20.8	-
EP_04	-	-	-	**1.2**	**1.9**	**1.7**	21.7	56.1	-	64.3	66.3	26.2	60.4	25.8	**1.5**	64.5	49.1	73.1
EP_05	-	-	-	66.0	17.1	72.8	-	-	-	28.2	74.7	64.0	47.0	63.4	41.7	64.2	58.3	446.2
EP_06	-	-	-	17.5	51.0	45.0	-	-	-	37.8	43.6	41.9	33.6	36.2	57.6	33.5	135.0	119.1
EP_07	-	-	-	**0.9**	**0.7**	**0.8**	-	-	-	45.9	43.6	111.8	38.3	14.1	57.8	106.0	58.9	-
EP_08	-	-	-	39.0	**3.5**	**0.6**	-	-	-	46.6	48.9	15.6	36.6	24.8	328.0	35.0	36.3	-
EP_09	-	-	-	32.8	**3.0**	**0.5**	64.3	-	-	41.8	25.1	26.4	48.3	111.1	28.2	34.9	37.8	-
EP_10	-	-	-	**2.5**	**1.9**	**1.6**	-	-	-	57.2	**7.4**	17.9	30.8	29.9	**3.3**	52.1	38.6	**6.1**
EP_11	-	-	-	**0.9**	**0.7**	**0.5**	-	-	-	63.6	25.1	44.3	44.7	24.0	**6.9**	35.6	**0.6**	47.0
EP_12	-	-	-	16.8	**0.9**	34.9	-	-	-	47.7	57.3	69.1	38.1	35.9	74.5	49.7	68.2	-
EP_13	-	-	-	**5.8**	**1.0**	**2.5**	-	-	-	36.0	63.1	-	116.0	63.6	17.9	50.6	46.3	-
EP_14	-	-	-	**1.4**	**1.3**	**1.9**	-	-	-	23.4	13.2	**2.1**	11.3	14.3	**1.3**	29.2	37.9	-
EP_15	-	-	-	51.1	42.8	54.0	-	-	-	49.6	33.4	26.5	41.4	61.7	55.9	54.6	63.6	-
EP_16	-	-	-	**1.9**	**2.2**	**2.2**	-	-	-	59.1	65.6	59.7	55.6	143.1	73.3	-	30.0	-
EP_17	-	-	-	23.8	33.9	**1.9**	-	-	-	29.2	25.6	27.0	25.4	92.3	45.6	71.8	136.0	-
EP_18	-	-	-	**1.3**	**3.9**	**1.3**	155.1	-	-	51.8	47.9	**2.1**	29.7	41.0	**2.3**	33.6	-	41.9
EP_19	-	-	-	39.0	56.1	20.2	-	-	-	63.9	42.9	63.2	47.1	56.9	34.1	60.2	51.5	43.5
EP_20	-	-	-	42.6	80.6	77.6	-	-	-	132.2	73.4	94.5	92.5	57.0	61.8	-	-	-

Table F.2: For the $I_{post} - I_{pre}$ image pair, these are all values of μ_D for the fully automatic algorithm registration in mm. For each of the algorithms, the images were run through the algorithm in full size, half size and quarter size. A missing value signifies that the algorithm was unable to estimate a transformation matrix due to insufficient matched features. A μ_D above 10 mm is printed as red and considered a total mismatch; μ_D values below that are printed in black and bold.

	FAST			**SURF**			**BRISK**			**Harris**			**MinEigen**			**MSER**		
	full	half	quarter	full	half	quarter	full	half	quarter	full	half	quarter	full	half	quarter	full	half	quarter
EP_01	-	-	-	40.8	41.9	**3.6**	-	-	-	70.7	69.0	333.8	38.1	81.0	53.8	52.1	42.0	-
EP_02	-	-	-	59.5	23.3	61.0	-	-	-	71.7	66.9	61.8	45.5	69.3	49.4	66.0	60.0	-
EP_03	-	-	-	30.0	38.4	34.7	-	-	-	45.7	37.7	79.6	65.8	24.5	53.6	49.7	-	-
EP_04	-	-	-	52.9	38.9	64.7	-	-	-	68.3	34.5	40.0	53.8	50.2	25.5	46.9	48.6	-
EP_05	-	-	-	56.6	69.9	31.8	-	-	-	35.2	66.0	188.2	66.1	58.6	88.7	51.6	354.4	-
EP_06	-	-	-	36.1	45.4	57.1	-	-	-	68.8	38.0	29.6	54.5	197.4	68.2	149.7	112.8	81.4
EP_07	-	-	-	47.6	44.0	193.5	-	-	-	53.3	52.4	100.2	59.2	44.4	83.9	49.3	76.7	35.9
EP_08	-	-	-	37.2	36.4	152.1	-	-	-	93.3	43.5	-	40.8	19.7	26.5	32.8	25.5	-
EP_09	-	-	-	18.0	42.7	41.6	348.6	-	-	42.7	47.5	19.0	37.3	156.8	22.7	25.7	63.0	-
EP_10	-	-	-	50.2	**7.6**	32.3	-	-	-	59.4	68.8	87.3	26.5	64.5	67.9	67.4	19.8	-
EP_11	-	-	-	34.4	**7.8**	**5.7**	-	-	-	34.1	37.3	23.3	59.9	193.3	60.5	57.6	-	29.0
EP_12	-	-	-	56.3	38.4	86.2	-	-	-	53.7	41.2	35.5	34.4	26.9	30.1	86.8	48.1	42.1
EP_13	-	-	-	41.5	28.8	50.9	-	-	-	60.9	56.5	29.5	38.3	57.3	72.8	47.1	125.4	100.0
EP_14	-	-	-	30.5	24.2	56.8	-	-	-	25.8	16.5	28.5	51.3	78.0	43.7	28.2	-	36.2
EP_15	-	-	-	41.6	43.5	28.4	-	-	-	54.6	35.1	31.5	32.4	44.4	49.2	47.5	38.4	46.5
EP_16	-	-	-	54.8	76.3	82.7	-	-	-	92.4	67.2	62.4	66.4	70.5	26.6	55.2	78.1	70.8
EP_17	-	-	-	45.1	56.8	41.2	-	-	-	40.9	85.7	28.2	91.1	36.1	57.4	107.3	107.2	-
EP_18	-	-	-	49.3	27.5	**1.8**	-	-	-	52.8	46.7	30.9	66.8	52.7	**6.5**	64.6	-	-
EP_19	-	-	-	46.3	39.4	32.8	-	-	-	65.2	63.0	26.2	55.0	566.8	11.6	73.4	72.1	-
EP_20	-	-	-	40.9	100.4	58.3	-	-	-	85.9	106.8	168.4	76.2	149.9	91.6	96.6	724.0	-

Bibliography

[1] Michel J. A. M. van Putten. *Essentials of Neurophysiology: Basic Concepts and Clinical Applications for Scientists and Engineers*. Springer-Verlag, Berlin Heidelberg, 2007.

[2] Robert S. Fisher, J. Helen Cross, Jacqueline A. French, Norimichi Higurashi, Edouard Hirsch, Floor E. Jansen, Lieven Lagae, Solomon L. Mosh??, Jukka Peltola, Eliane Roulet Perez, Ingrid E. Scheffer, and Sameer M. Zuberi. Operational classification of seizure types by the International League Against Epilepsy: Position Paper of the ILAE Commission for Classification and Terminology. *Epilepsia*, 58(4):522–530, 2017.

[3] WHO. Epilepsy fact sheet. URL: http://www.who.int/mediacentre/factsheets/fs999/en/, 2017.

[4] Erik K St Louis, William E Rosenfeld, and Thomas Bramley. Antiepileptic Drug Monotherapy : The Initial Approach in Epilepsy Management. pages 77–82, 2009.

[5] Emilio Perucca and Torbjörn Tomson. The pharmacological treatment of epilepsy in adults. *The Lancet Neurology*, 10(5):446–456, 2011.

[6] Tracy Glauser, Elinor Ben-Menachem, Blaise Bourgeois, Avital Cnaan, David Chadwick, Carlos Guerreiro, Reetta Kalviainen, Richard Mattson, Emilio Perucca, and Torbjorn Tomson. ILAE treatment guidelines: Evidence-based analysis of antiepileptic drug efficacy and effectiveness as initial monotherapy for epileptic seizures and syndromes. *Epilepsia*, 47(7):1094–1120, 2006.

[7] Patrick Kwan, Alexis Arzimanoglou, Anne T. Berg, Martin J. Brodie, W. Allen Hauser, Gary Mathern, Solomon L. Moshé, Emilio Perucca, Samuel Wiebe, and Jacqueline French. Definition of drug resistant epilepsy: Consensus proposal by the ad hoc Task Force of the ILAE Commission on Therapeutic Strategies. *Epilepsia*, 51(6):1069–1077, 2010.

[8] Patrick Kwan and Martin J. Brodie. Early Identification of Refractory Epilepsy. *New England Journal of Medicine*, 342(5):314–319, 2000.

[9] Barbara C. Jobst and Gregory D. Cascino. Resective Epilepsy Surgery for Drug-Resistant Focal Epilepsy. *Jama*, 313(3):285, 2015.

[10] Hans O. Lüders, Imad Najm, Dileep Nair, Peter Widdess-Walsh, and William Bingman. The epileptogenic zone: General principles. *Epileptic Disorders*, 8(SUPPL. 2):1–9, 2006.

[11] Maeike Zijlmans, Premysl Jiruska, Rina Zelmann, S S Frans, John G R Jefferys, and Jean Gotman. High-Frequency Oscillations as a New Biomarker in Epilepsy. 71(2):169–178, 2012.

[12] J. Jacobs, R. Staba, E. Asano, H. Otsubo, J. Y. Wu, M. Zijlmans, I. Mohamed, P. Kahane, F. Dubeau, V. Navarro, and J. Gotman. High-frequency oscillations (HFOs) in clinical epilepsy. *Progress in Neurobiology*, 98(3):302–315, 2012.

[13] Dileep R. Nair, Richard Burgess, Cameron C. McIntyre, and Hans Lüders. Chronic subdural electrodes in the management of epilepsy. *Clinical Neurophysiology*, 119(1):11–28, 2008.

[14] Felix Rosenow and Hans Lüders. Presurgical evaluation of epilepsy. *Brain*, 124:1683–1700, 2001.

[15] Marco De Curtis and Giuliano Avanzini. Interictal spikes in focal epileptogenesis. *Progress in Neurobiology*, 63:541–567, 2001.

[16] M Anderson, G Alarco, J J Garcõ, Âa Seoane, R Selway, C D Binnie, and A Valentõ. Responses to single pulse electrical stimulation identify epileptogenesis in the human brain in vivo. 2002.

[17] C J Stam, P Tewarie, E Van Dellen, E C W Van Straaten, A Hillebrand, and P Van Mieghem. The trees and the forest : Characterization of complex brain networks with minimum spanning trees. *International Journal of Psychophysiology*, 92(3):129–138, 2014.

[18] Ida A. Nissen, Cornelis J. Stam, Jaap C. Reijneveld, Ilse E C W van Straaten, Eef J. Hendriks, Johannes C. Baayen, Philip C. De Witt Hamer, Sander Idema, and Arjan Hillebrand. Identifying the epileptogenic zone in interictal resting-state MEG source-space networks. *Epilepsia*, 58(1):137–148, 2017.

[19] Alex Fornito, Andrew Zalesky, and Edward Bullmore. *Fundamentals of brain network analysis*. Academic Press, 2016.

[20] Steven H. Strogatz. Exploring complex networks. *Nature*, 410(6825):268–276, 2001.

[21] Santiago Ramón y Cajal. *Les nouvelles idées sur la structure du système nerveux chez l'homme et chez les vertébrés*. Paris, 1894.

[22] Pascal Fries. A mechanism for cognitive dynamics : neuronal communication through neuronal coherence. *TRENDS in Cognitive Sciences*, 9(10), 2005.

[23] Ed Bullmore and Olaf Sporns. Complex brain networks: graph theoretical analysis of structural and functional systems. *Nature Reviews Neuroscience*, 10(4):312–312, 2009.

[24] Olaf Sporns, Giulio Tononi, and Rolf Kötter. The human connectome: A structural description of the human brain. *PLoS Computational Biology*, 1(4):0245–0251, 2005.

[25] György Buzsáki, Costas A. Anastassiou, and Christof Koch. The origin of extracellular fields and currents-EEG, ECoG, LFP and spikes. *Nature Reviews Neuroscience*, 13(6):407–420, 2012.

[26] M J Kamiński and K J Blinowska. A new method of the description of the information flow in the brain structures. *Biological cybernetics*, 65(3):203–210, 1991.

[27] Xiaoqian Sun, Volker Gollnick, and Sebastian Wandelt. Robustness analysis metrics for worldwide airport network: A comprehensive study. *Chinese Journal of Aeronautics*, 30(2):500–512, 2017.

[28] Tore Opsahl, Filip Agneessens, and John Skvoretz. Node centrality in weighted networks: Generalizing degree and shortest paths. *Social Networks*, 32(3):245–251, 2010.

[29] Mikail Rubinov and Olaf Sporns. Complex network measures of brain connectivity: Uses and interpretations. *NeuroImage*, 52(3):1059–1069, 2010.

[30] Stefano Boccaletti, V. Latora, Y. Moreno, M. Chavez, and D. U. Hwang. Complex networks: Structure and dynamics. *Physics Reports*, 424(4-5):175–308, 2006.

[31] Kurt Bryan and Tanya Leise. The $25,000,000,000 Eigenvector: The Linear Algebra behind Google. *SIAM Review*, 48(3):569–581, 2006.

[32] Fabrice Bartolomei, Stanislas Lagarde, Fabrice Wendling, and Aileen Mcgonigal. Defining epileptogenic networks : Contribution of SEEG and signal analysis. pages 1131–1147, 2017.

[33] S. C. Ponten, F. Bartolomei, and C. J. Stam. Small-world networks and epilepsy: Graph theoretical analysis of intracerebrally recorded mesial temporal lobe seizures. *Clinical Neurophysiology*, 118(4):918–927, 2007.

[34] Seung Hyun Jin, Woorim Jeong, and Chun Kee Chung. Mesial temporal lobe epilepsy with hippocampal sclerosis is a network disorder with altered cortical hubs. *Epilepsia*, 56(5):772–779, 2015.

[35] N.A. Crossley, A. Mechelli, J. Scott, F. Carletti, Peter T Fox, P McGuire, and Edward Bullmore. The hubs of the human connectome are generally implicated in the anatomy of brain disorders. *Brain*, 137:2382–2395, 2014.

[36] Boris C. Bernhardt, Zhang Chen, Yong He, Alan C. Evans, and Neda Bernasconi. Graph-theoretical analysis reveals disrupted small-world organization of cortical thickness correlation networks in temporal lobe epilepsy. *Cerebral Cortex*, 21(9):2147–2157, 2011.

[37] Jurgen Hebbink, Hil Meijer, Geertjan Huiskamp, Stephan van Gils, and Frans Leijten. Phenomenological network models: Lessons for epilepsy surgery. *Epilepsia*, 58(10):e147–e151, 2017.

[38] M Goodfellow, C Rummel, E Abela, M P Richardson, K Schindler, and J R Terry. Estimation of brain network ictogenicity predicts outcome from epilepsy surgery. *Nature Publishing Group*, (April):1–13, 2016.

[39] Zhiqiang Zhang, Wei Liao, Huafu Chen, Dante Mantini, Ju Rong Ding, Qiang Xu, Zhengge Wang, Cuiping Yuan, Guanghui Chen, Qing Jiao, and Guangming Lu. Altered functional-structural coupling of large-scale brain networks in idiopathic generalized epilepsy. *Brain*, 134(10):2912–2928, 2011.

[40] Ida A. Nissen, Nicole E C van Klink, Maeike Zijlmans, Cornelis J. Stam, and Arjan Hillebrand. Brain areas with epileptic high frequency oscillations are functionally isolated in MEG virtual electrode networks. *Clinical Neurophysiology*, 127(7):2581–2591, 2016.

[41] Edwin Van Dellen, Linda Douw, Arjan Hillebrand, Philip C. de Witt Hamer, Johannes C. Baayen, Jan J. Heimans, Jaap C. Reijneveld, and Cornelis J. Stam. Epilepsy surgery outcome and functional network alterations in longitudinal MEG: A minimum spanning tree analysis. *NeuroImage*, 86:354–363, 2014.

[42] Eric van Diessen, Willem M. Otte, Kees P.J. Braun, Cornelis J. Stam, and Floor E. Jansen. Improved Diagnosis in Children with Partial Epilepsy Using a Multivariable Prediction Model Based on EEG Network Characteristics. *PLoS ONE*, 8(4), 2013.

[43] Guillermo J. Ortega, Rafael G. Sola, and Jesús Pastor. Complex network analysis of human ECoG data. *Neuroscience Letters*, 447(2-3):129–133, 2008.

[44] Christopher Wilke, Gregory Worrell, and Bin He. Graph analysis of epileptogenic networks in human partial epilepsy. *Epilepsia*, 52(1):84–93, 2011.

[45] Mark A Kramer, Eric D Kolaczyk, and Heidi E Kirsch. Emergent network topology at seizure onset in humans. 2008.

[46] Bartosz T. Grobelny, Dennis London, Travis C. Hill, Emily North, Patricia Dugan, and Werner K. Doyle. Betweenness centrality of intracranial electroencephalography networks and surgical epilepsy outcome. *Clinical Neurophysiology*, 129(9):1804–1812, 2018.

[47] Pieter Van Mierlo, Evelien Carrette, Hans Hallez, Robrecht Raedt, Alfred Meurs, Stefaan Vandenberghe, Dirk Van Roost, Paul Boon, Steven Staelens, and Kristl Vonck. Ictal-onset localization through connectivity analysis of intracranial EEG signals in patients with refractory epilepsy. *Epilepsia*, 54(8):1409–1418, 2013.

[48] Christopher Wilke, Gregory A. Worrell, and Bin He. Analysis of epileptogenic network properties during ictal activity. *Proceedings of the 31st Annual International Conference of the IEEE Engineering in Medicine and Biology Society: Engineering the Future of Biomedicine, EMBC 2009*, pages 2220–2223, 2009.

[49] Giulia Varotto, Laura Tassi, Silvana Franceschetti, Roberto Spreafico, and Ferruccio Panzica. Epileptogenic networks of type II focal cortical dysplasia: A stereo-EEG study. *NeuroImage*, 61(3):591–598, 2012.

[50] Sandra Courtens, Bruno Colombet, Agnès Trébuchon, Andrea Brovelli, Fabrice Bartolomei, and Christian G. Bénar. Graph Measures of Node Strength for Characterizing Preictal Synchrony in Partial Epilepsy. *Brain Connectivity*, 6(7):530–539, 2016.

[51] Yonathan Murin, Jeremy Kim, Josef Parvizi, and Andrea Goldsmith. SozRank: A new approach for localizing the epileptic seizure onset zone. *PLoS Computational Biology*, 14(1):1–26, 2018.

[52] Samuel P. Burns, Sabato Santaniello, Robert B. Yaffe, Christophe C. Jouny, Nathan E. Crone, Gregory K. Bergey, William S. Anderson, and Sridevi V. Sarma. Network dynamics of the brain and influence of the epileptic seizure onset zone. *Proceedings of the National Academy of Sciences*, 111(49):E5321–E5330, 2014.

[53] Eric Van Diessen, Judith I. Hanemaaijer, Willem M. Otte, Rina Zelmann, Julia Jacobs, Floor E. Jansen, François Dubeau, Cornelis J. Stam, Jean Gotman, and Maeike Zijlmans. Are high frequency oscillations associated with altered network topology in partial epilepsy? *NeuroImage*, 82:564–573, 2013.

[54] Dora Hermes, Kai J. Miller, Herke Jan Noordmans, Mariska J. Vansteensel, and Nick F. Ramsey. Automated electrocorticographic electrode localization on individually rendered brain surfaces. *Journal of Neuroscience Methods*, 185(2):293–298, 2010.

[55] Mariana P. Branco, Anna Gaglianese, Daniel R. Glen, Dora Hermes, Ziad S. Saad, Natalia Petridou, and Nick F. Ramsey. ALICE: A tool for automatic localization of intra-cranial electrodes for clinical and high-density grids. *Journal of Neuroscience Methods*, 301:43–51, 2018.

[56] Gabriele Arnulfo, Massimo Narizzano, Francesco Cardinale, Marco Massimo Fato, and Jaakko Matias Palva. Automatic segmentation of deep intracerebral electrodes in computed tomography scans. *BMC Bioinformatics*, 16(1):1–12, 2015.

[57] Ian J. Gerard, Marta Kersten-Oertel, Kevin Petrecca, Denis Sirhan, Jeffery A. Hall, and D. Louis Collins. Brain shift in neuronavigation of brain tumors: A review. *Medical Image Analysis*, 35:403–420, 2017.

[58] Barbara Zitová and Jan Flusser. Image registration methods: A survey. *Image and Vision Computing*, 21(11):977–1000, 2003.

[59] Leila MG Fonseca and Max HM Costa. Automatic Registration of Satellite Images. In *X Brazilian Symposium on Computer Graphics and Image Processing*, pages 219–226, 1997.

[60] J B Maintz and M A Viergever. A survey of medical image registration. *Medical image analysis*, 2(1):1–36, 1998.

[61] Max A. Viergever, J. B.Antoine Maintz, Stefan Klein, Keelin Murphy, Marius Staring, and Josien P.W. Pluim. A survey of medical image registration – under review. *Medical Image Analysis*, 33:140–144, 2016.

[62] Mark J. Boogers, Alexander Broersen, Joëlla E. Van Velzen, Fleur R. De Graaf, Heba M. El-Naggar, Pieter H. Kitslaar, Jouke Dijkstra, Victoria Delgado, Eric Boersma, Albert De Roos, Joanne D. Schuijf, Martin J. Schalij, Johan H.C. Reiber, Jeroen J. Bax, and J. Wouter Jukema. Automated quantification of coronary plaque with computed tomography: Comparison with intravascular ultrasound using a dedicated registration algorithm for fusion-based quantification. *European Heart Journal*, 33(8):1007–1016, 2012.

[63] B Bach Cuadra, Claudio Pollo, Anton Bardera, Olivier Cuisenaire, and J P Thiran. Atlas-Based Segmentation of Pathological Brain {MR} Images using a model of lesion growth. *IEEE Trans. Med. Imaging*, 23(10):1301–1314, 2004.

[64] Sarang S. Dalal, Erik Edwards, Heidi E. Kirsch, Nicholas M. Barbaro, Robert T. Knight, and Srikantan S. Nagarajan. Localization of neurosurgically implanted electrodes via photograph-MRI-radiograph coregistration. *Journal of Neuroscience Methods*, 174(1):106–115, 2008.

[65] James T. Rutka, Hiroshi Otsubo, Shouhei Kitano, Hiroaki Sakamoto, Atsushi Shirasawa, Ayako Ochi, and O. Carter Snead. Utility of digital camera-derived intraoperative images in the planning of epilepsy surgery for children. *Neurosurgery*, 45(5):1186–1191, 1999.

[66] Susan Spencer and Linda Huh. Long-term outcomes of epilepsy surgery in adults and children. *Outcomes of Epilepsy Surgery in Adults and Children*, 7(June):525–37, 2008.

[67] Juan C. Bulacio, Lara Jehi, Chong Wong, Jorge Gonzalez-Martinez, Prakash Kotagal, Dileep Nair, Imad Najm, and William Bingaman. Long-term seizure outcome after resective surgery in patients evaluated with intracranial electrodes. *Epilepsia*, 53(10):1722–1730, 2012.

[68] Nicole E C van Klink. *High Frequency Oscillations in Epilepsy: Towards Clinical Applications*. PhD thesis, University of Utrecht, 2017.

[69] Jerome Engel. *Surgical Treatment of the Epilepsies*. Lippincott Williams & Wilkins, 1993.

[70] Gideon Schwarz. Estimating the dimension of a model. *The Annals of Statistics*, 6(2):461–464, 1978.

[71] Jack McKay Fletcher and Thomas Wennekers. From Structure to Activity: Using Centrality Measures to Predict Neuronal Activity. *International Journal of Neural Systems*, 27(0):1750013, 2016.

[72] Robert Oostenveld, Pascal Fries, Eric Maris, and Jan-Mathijs Schoffelen. FieldTrip: Open Source Software for Advanced Analysis of MEG, EEG, and Invasive Electrophysiological Data. *Computational Intelligence and Neuroscience*, 2011:1–9, 2011.

[73] E. van Diessen, T. Numan, E. van Dellen, A. W. van der Kooi, M. Boersma, D. Hofman, R. van Lutterveld, B. W. van Dijk, E. C.W. van Straaten, A. Hillebrand, and C. J. Stam. Opportunities and methodological challenges in EEG and MEG resting state functional brain network research. *Clinical Neurophysiology*, 126(8):1468–1481, 2015.

[74] Katarzyna J. Blinowska. Review of the methods of determination of directed connectivity from multichannel data. *Medical and Biological Engineering and Computing*, 49(5):521–529, 2011.

[75] Anna Korzeniewska, Małgorzata Mańczak, Maciej Kamiński, Katarzyna J. Blinowska, and Stefan Kasicki. Determination of information flow direction among brain structures by a modified directed transfer function (dDTF) method. *Journal of Neuroscience Methods*, 125(1-2):195–207, 2003.

[76] A. Korzeniewska. Ictal propagation of high frequency activity is recapitulated in interictal recordings: effective connectivity of epileptogenic networks recorded with intracranial EEG. *Neuroim*, (101):96–113, 2014.

[77] Abraham Kuruvilla and Roland Flink. Intraoperative electrocorticography in epilepsy surgery: Useful or not? *Seizure*, 12(8):577–584, 2003.

[78] Thomas A Pieters, Christopher R Conner, and N Tandon. Recursive grid partitioning on a cortical surface model: an optimized technique for the localization of implanted subdural electrodes. *Journal of Neurosurgery*, 118(5):1086–1097, 2013.

[79] James P. O'Shea, William M. Wells III, and Alexandra J. Golby. Using surface normals to localize subdural intracranial electrodes placed during neurosurgery. *ISBI*, pages 331–334, 2006.

[80] J. P. Thirion. Image matching as a diffusion process: An analogy with Maxwell's demons. *Medical Image Analysis*, 2(3):243–260, 1998.

[81] C W J Granger. Investigating Causal Relations by Econometric Models and Cross-spectral Methods. *Econometrica*, 37(3):424–438, 1969.

[82] Tapio Schneider and Arnold Neumaier. Algorithm 808: ARfit—a matlab package for the estimation of parameters and eigenmodes of multivariate autoregressive models. *ACM Transactions on Mathematical Software*, 27(1):58–65, 2001.

[83] Arnold Neumaier and Tapio Schneider. Estimation of parameters and eigenmodes of multivariate autoregressive models. *ACM Transactions on Mathematical Software*, 27(1):27–57, 2001.

[84] Sergey Brin and Lawrence Page. The Anatomy of a Large-Scale Hypertextual Web Search Engine. In *Seventh International World-Wide Web Conference*, 1998.

[85] Massimo Franceschet. PageRank : Standing on the Shoulders of Giants. *Communications of the ACM*, 54(6):92–101, 2011.